RSC Advances

PAPER

Published on 17 August 2026

Cite this: DOI: 10.1039/d6ra03722d

Click chemistry-based synthesis of fluorescent digitoxin derivatives with anticancer activity and cellular imaging potential

Jiří Bejček,[a] Michal Jurášek,*[b] Monika Kreisslová,[a] Jan Škubník,[a] Ivana Křížová,[c] Jan Fähnrich,[d] Soňa Gurská,[e] Petr Džubák,[e] Marián Hajdúch,[e] Vojtěch Spiwok,[a] Pavel Drašar,[b] Tomáš Ruml[a] and Silvie Rimpelová *[a]

Cardiac glycosides are secondary plant metabolites with considerable potential as therapeutic agents in cancer treatment. However, digitoxin (**Dg**), one of the most studied members of this class, is reported to exhibit dose-limiting systemic toxicity and cannot be directly tracked in cancer cells. To address these limitations, we investigated whether **Dg** derivatization and conjugation with fluorescent moieties could modulate its cytotoxic profile *in vitro* while enabling cellular imaging. Such dual-function compounds may provide useful tools for studying the intracellular behavior of **Dg** derivatives while retaining anticancer activity. In this study, we designed and synthesized fluorescently labelled **Dg** derivatives *via* conjugation with BODIPY, Nile red, fluorescein, fluorescein isothiocyanate (**F9**), coumarin, rhodamine, and tetramethylrhodamine (**F10**) using copper-catalyzed click chemistry. To determine whether these derivatives retained interaction with Na^+/K^+-ATPase, molecular docking and molecular dynamics simulations were performed, confirming stable complexes for selected lead compounds. We then evaluated 72-h cytotoxicity of the new **Dg** derivatives in lung adenocarcinoma (A549), noncancerous lung fibroblasts (MRC-5), and several additional cancer cell lines. Overall cytotoxicity decreased 5–49-fold relative to **Dg**, with **FD10** and **FD9** retaining the highest activity. Fluorescence microscopy revealed intracellular localization of the derivatives in the endoplasmic reticulum, lysosomes, and cytoplasmic membrane in both A549 and MRC-5 cells. To further assess their effects in a more advanced model, **Dg** derivatives were evaluated in A549 cancer cell spheroids. Morphological changes were observed, with **FD10** and **FD9** inducing the greatest reduction in spheroid compactness after 3 and 17 days. Additionally, apoptosis was identified as the predominant mode of cell death in A549 cells treated with **FD9** and **FD10** after 48 h. Overall, these findings suggest that fluorescent **Dg** derivatives represent promising candidates for further development as anticancer agents with integrated imaging capability as tools for studying the cellular distribution of **Dg**-based tumor compounds.

Received 1st May 2026
Accepted 26th July 2026

DOI: 10.1039/d6ra03722d

rsc.li/rsc-advances

1 Introduction

For centuries, secondary metabolites derived from plants and fungi have been widely used to treat numerous diseases. Over time, remedies that initially began as crude extracts have evolved into sophisticated pharmaceutical formulations designed for targeted medical applications. While these remedies have led to great medical breakthroughs, to this day, some diseases remain difficult to control, with cancer being a notable example. Today, cancer is the leading cause of death worldwide,[1] and despite predictions of a decline in its mortality rate,[2,3] the demand for new therapeutic approaches persists. In addition to traditional drug development, an alternative strategy known as drug repositioning can be utilized. This faster and more cost-effective approach[4,5] is currently being applied for cardiac glycosides (CGs).

CGs represent a diverse group of substances of plant origin and although numerous cellular targets for CGs have been identified over the years, their primary mode of action is still considered to be the inhibition of Na^+/K^+-ATPase (NKA), which is associated with a subsequent increase in intracellular Ca^{2+}

[a]*Department of Biochemistry and Microbiology, University of Chemistry and Technology, Prague, Technická 3, Prague 6, 166 28, The Czech Republic. E-mail: silvie.rimpelova@vscht.cz*

[b]*Department of Chemistry of Natural Compounds, University of Chemistry and Technology, Prague, Technická 5, Prague 6, 166 28, The Czech Republic. E-mail: michal.jurasek@vscht.cz*

[c]*Department of Biotechnology, University of Chemistry and Technology, Prague, Technická 5, Prague 6, 166 28, The Czech Republic*

[d]*Department of Analytical Chemistry, University of Chemistry and Technology, Prague, Technická 5, Prague 6, 166 28, The Czech Republic*

[e]*Laboratory of Experimental Medicine, Institute of Molecular and Translational Medicine, Faculty of Medicine and Dentistry, Palacky University and University Hospital Olomouc, Hnevotinska 5, Olomouc, 775 20, Czech Republic*

concentration.[6] This mechanism has secured their approval as drugs for the treatment of heart failure and cardiac arrhythmias. However, the interaction of CGs with NKA involves more than just NKA inhibition and ion balance disruption.

It is known that, at low concentrations, CGs activate the NKA signalosome, which can lead to several downstream effects: (i) transactivation of the epidermal growth factor receptor *via* activated non-receptor tyrosine kinase (Src), resulting in the activation of the Ras/Raf/MEK/MAPK signaling pathway,[7–9] (ii) activation of phospholipase C, again *via* activated Src, leading to Ca^{2+} oscillations,[10–12] (iii) activation of phosphatidylinositol-3-kinase, which is Src-independent and promotes NKA internalization.[13] The reasons for specific activation of these pathways are complex and likely depend on the structure of each CG[14] and the type of cell involved.[11,15]

One of the key members of the CG family is digoxin, which is widely used in clinical treatments. However, a major drawback of digoxin is its renal excretion, making it potentially hazardous for patients with renal failure.[16] A possible and clinically interesting alternative is **Dg**, a structurally similar compound, the elimination of which is not affected by renal function. **Dg** is known for inducing apoptosis in various human cancer cell lines, including lung (NCI-H460)[17] and colon (SW480)[18] cancer cells, malignant hematological cells,[19] and cells from hepatocellular carcinoma (HepG2).[20] Although **Dg** exhibits cytotoxic effects in a wide range of tumor cells at low nanomolar concentrations,[9,21] with particularly strong activity against lung adenocarcinoma, further studies are needed to elucidate its mechanism of action.[22] Additionally, its cytotoxic properties can be further modulated by derivatization of the carbohydrate skeleton.[22,23] Moreover, introducing a fluorescent molecule to **Dg** enables to study its intracellular localization, as previously demonstrated with other natural compounds, such as colchicine, trilobolide, or archangelolide.[24–26]

One potential fluorophore for **Dg** derivatization is boron-dipyrromethene (BODIPY), a widely used fluorescent label known for its low toxicity and high quantum yields.[27–29] BODIPY has been effectively used to explore the biological properties of other CGs, such as ouabain[30–34] and oleandrin.[35,36] However, to the best of our knowledge, no studies have investigated the conjugation of **Dg** with BODIPY or other fluorescent dyes such as Nile red, coumarin, rhodamine, or fluorescein.

For this reason, in this study, we synthesized conjugates of **Dg** with BODIPY and the aforementioned fluorophores using copper-catalyzed click chemistry and evaluated their biological activity in various mammalian cell lines. Molecular docking and molecular dynamics confirmed their interactions with NKA. All derivatives were less cytotoxic compared to **Dg** and their IC_{50} in hundreds of nanomoles per liter after 72-h incubation in both 2D cancerous and noncancerous cells. Next, fluorescence microscopy revealed the impact of **Dg** derivatization on its intracellular localization, which was mostly in endoplasmic reticulum and lysosomes. Moreover, most of the derivatives were able to retain their cytotoxicity even in a 3D model (cell spheroids). Flow cytometry confirmed the proapoptotic effects of the **Dg** derivatives in A549 cells. Overall, our newly synthesized **Dg** derivatives exhibited promising anticancer properties against lung cancer cells.

2 Results

The aim of this study was to design and synthesize new **Dg** derivatives with varying fluorescent labels and to evaluate their suitability for potential theranostic applications. Since these labels can significantly influence the biological activity of the derivatives, including their intracellular distribution and interaction with their molecular target, NKA. Therefore, to assess how the behavior of the new derivatives differs from that of **Dg**, we employed a combination of *in silico* and *in vitro* methods.

2.1 Synthesis of digitoxin derivatives

2.1.1 Chemistry. The preparation of fluorescent derivatives of digitoxin (**Dg**) is shown in Fig. 1. The proposed synthetic approach consists of azidoalkyne cycloaddition (CuAAC) of an azido-terminated analogue (**DgA**) and alkynylated fluorescent reporters (**F1–F10**; systematic names are in SI in Fig. S0). The preparation of the azide analogue **Dg** was based on the described approach of transformation of the terminal digitoxose[37,38] (2,6-dideoxy-D-d-*ribo*-hexopyranose) to a tertiary amine by reductive amination of the dialdehyde with [3-(azidomethyl)-5-hydroxyphenyl]methanamine (**AP**, see Fig. 1A). The **AP** precursor was designed to contain a hydroxyl group that could partially substitute for the elimination of the hydroxyl groups of digitoxose during the synthesis of **DgA**. **AP** was prepared from the corresponding diazide[39] by Staudinger reduction in the triphenylphosphine/water/THF system. The low yield of **AP** (38%) was due not only to the formation of the diamine but also to losses during chromatographic separation.

The synthetic transformation of **Dg** involved selective oxidation of the *cis*-diol to the terminal digitoxose with sodium periodate and subsequent reductive amination of the crude dialdehyde with **AP** using sodium cyanoborohydride as the reducing agent in the presence of acetic acid (Fig. 1A). Both of these steps are performed in tandem without isolation of the unstable dialdehyde. The presence of this intermediate was confirmed by mass analysis. The two-step transformation of the sugar resulted in a 7-membered heterocycle (2-methyl-1,4-oxazepane) containing a phenol bridge with a terminal azide group attached as a tertiary amine. **DgA** was readily isolated chromatographically as a pure compound in 59% yield.

The selected fluorophores are characterized by different emission bands and preferential intracellular localization. The syntheses of fluorescent alkynes **F1**,[40] **F2**,[41] **F5**,[42] **F6**,[43] **F7**,[44] **F8** (ref. 45) and **F9** (ref. 46) have been described in the literature previously (structures are given in SI, Fig. S1). TAMRA-alkyne (5(6)-carboxytetramethylrhodamine, **F10**) was commercially available. BODIPY alkynes **F3** and **F4** were prepared by Knoevenagel reaction from the corresponding aldehydes (4-dimethylaminobenzaldehyde, 3-hydroxybenzaldehyde) and BODIPY **F2** (Fig. 1B). The reactions were performed in an established manner using the catalytic system of piperidine and

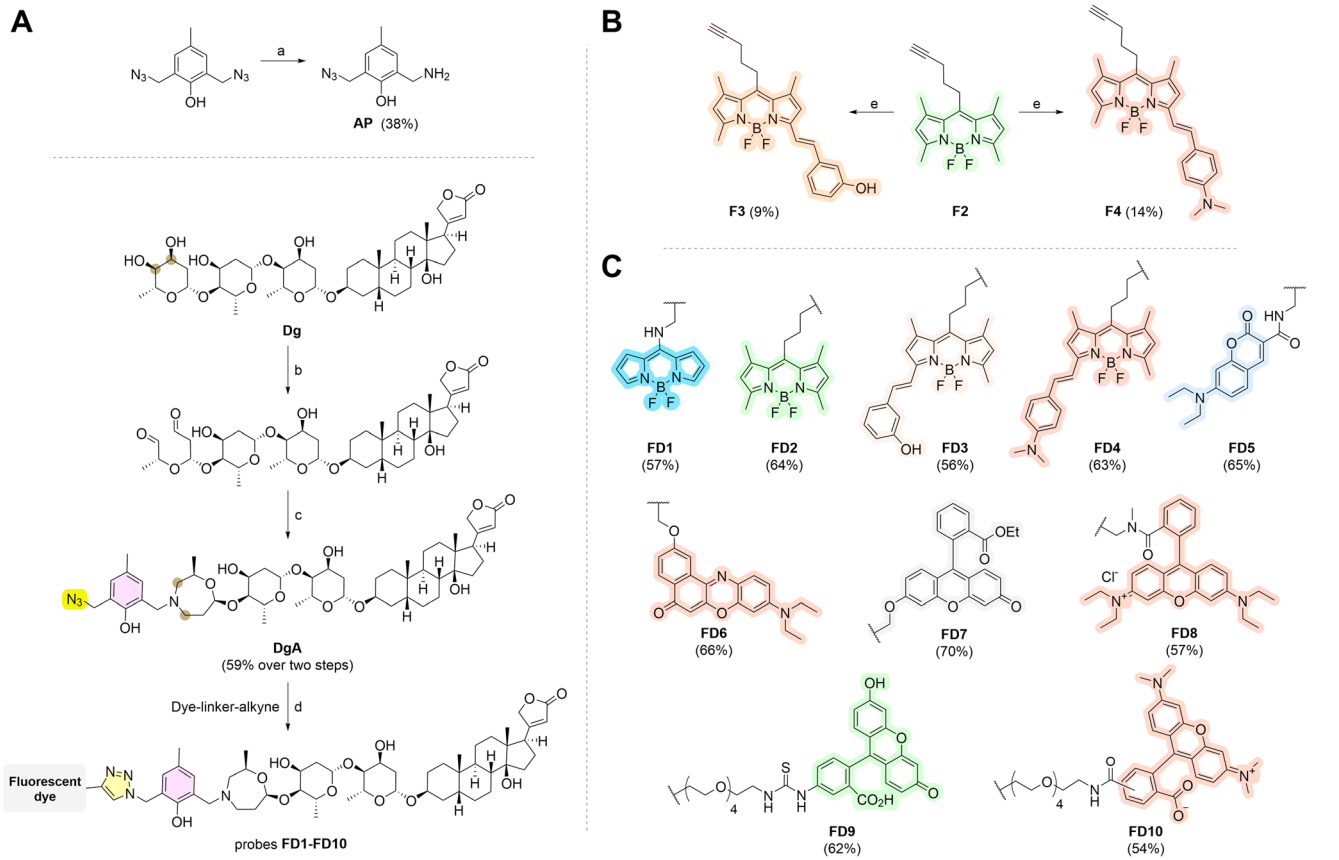

Fig. 1 (A) Synthetic route to fluorescent digitoxin probes (FDs); (B) preparation of new BODIPY dyes, and (C) structures of fluorescent dyes attached to a cardenolide. Reagents and conditions: (a) PPh_3, THF, H_2O, RT, ON; (b) MeOH, H_2O, $CHCl_3$, $NaIO_4$, RT, ON; (c) AP, HOAc, $NaCNBH_3$, MeOH, MS-4Å, RT, 1 h; (d) $CuSO_4 \cdot 5H_2O$ (aq), sodium ascorbate (aq), DMF, TBTA, RT, ON; (e) piperidine, HOAc, benzene, MW 120 °C, 1 h.

acetic acid in benzene. In our case, the reactions were performed under microwave conditions (MW; 1 h, 120 °C), however, the product yields reached rather usual values[47,48] (for **F3** 9%, for **F4** 14%).

The azido-terminated derivative of **DgA** and alkynylated derivatives of the fluorophores **F1–F10** were used to synthesize a series of fluorescent derivatives of **Dg** using a copper-catalyzed click reaction (Fig. 1C). The reaction results in an *in vivo* non-hydrolysable coupling of the reactants in the form of 1,4-disubstituted 1,2,3-triazoles. Perhaps for this reason, it is very popular in the field of natural product modification.[49] The reactions were carried out in a well-established catalytic system using the *in situ* reduction of divalent copper ($CuSO_4 \cdot 5H_2O$) with sodium ascorbate in the presence of tris((1-benzyl-4-triazolyl)methyl)amine (TBTA). A total of ten fluorescent derivatives (**FD1–FD10**) were prepared in good isolated yields (54–70%). The identity of the new compounds was confirmed by ^1H and ^{13}C NMR and mass spectra (HRMS-ESI/LRMS-ESI) and the purity of the compounds was verified by HPLC (purity of FDs was ≥95%). All processed data from these analyses are available in SI (Fig. S2–S16).

The conjugates were further characterized photochemically (Table 1). The spectra are presented in SI Fig. S16 and show the absorption coefficient calculated from a more concentrated solution measured in an absorption cell. For comparison, the absorption coefficient calculated from the absorption spectrum of the solution used for fluorescence measurements is also plotted. The corrected excitation and emission curves are in relative unitless values. The fluorescence emission is partially polarized. The average anisotropy values measured in the first absorption band are summarized in Table 2. However, polarization was not taken into account by spectral corrections and quantum yield estimation.

2.2 Molecular docking

Before conducting the *in vitro* tests, we utilized molecular docking to rapidly assess noncovalent interactions between the studied ligands and their target protein. The primary biding target of CGs is NKA, with the binding pocket located in the transmembrane domain between helices αM_1–αM_6. This pocket is accessible from the extracellular space, meaning ligands do not need to cross cell membranes to bind.

Moreover, the binding pocket is divided into two regions based on the distribution of amino acids on its surface: a hydrophilic region (Asp_{121}, Asn_{122}, and Thr_{797}) and a hydrophobic region (Ile_{315}, Phe_{316}, Gly_{319}, Phe_{783}, Phe_{786}, and Leu_{793}). Given that **Dg** is a well-known and studied ligand of NKA, we used its structure as a foundation to design new derivatives.

Table 1 Absorption and fluorescence characteristics of studied compounds

Compd	λ_{Amax} [nm]	ε [L mol^{-1} cm^{-1}]	λ_{Fmax} [nm]	Y_f	λ_{Ex} [nm]	λ_{Em} [nm]
FD1[a]	398	26 900	450	0.078	320, 331, 400	443, 453, 463
FD2[a]	496	117 000	505	0.652	380, 471, 499	497, 507, 517, 541
FD3[a]	557	102 000	566	0.696	320, 522, 560	557, 567, 577, 611
FD4[a]	600	64 800	737	>0.14[c]	384, 432, 590, 603	690, 724
FD5[a]	419	39 600	469	0.080	290, 324, 422	461, 471, 481
FD6[a]	549	40 800	631	0.659	326, 340, 548	620, 630, 640
FD7[a]	456	23 100	559	0.027	312, 353, 433, 459, 490	520, 530, 540, 558
FD8[a]	567	81 900	591	0.316	415, 531, 550, 570	571, 581, 591
FD9[b]	492	52 300	517	0.308	290, 463, 480, 494	508, 518, 528
FD10[b]	353	14 500	579	0.227	308, 356, 523, 555	560, 570, 580, 620

[a] Spectra measured in DMSO. [b] Spectra measured in PBS. [c] Long-wavelength part of emission spectrum is out of instrument range. λ_{Amax}, ε – wavelength and absorption coefficient at absorption maximum, λ_{Fmax} – wavelength of maximum of corrected emission spectra, Y_f – relative quantum yield of fluorescence, λ_{Ex}, λ_{Em} – wavelengths at which emission and excitation spectra were recorded. Excitation wavelengths for which quantum yields were evaluated are underlined.

Table 2 Average values and standard deviations of fluorescence anisotropy r in DMSO or PBS at 28 °C for studied compounds at specified excitation/emission wavelength

Compd	r	SD(r)	Wavelength [nm]
FD1[a]	0.098	0.004	400/453, 463
FD2[a]	0.019	0.001	499/507, 517, 547
FD3[a]	0.047	0.002	560/567, 577, 611
FD4[a]	0.131	0.008	603/690, 724, 740
FD5[a]	0.212	0.003	422/461, 471, 486
FD6[a]	0.041	0.001	556/620, 630, 640
FD7[a]	0.199	0.015	459, 490/520, 530, 540, 558
FD8[a]	0.107	0.003	570/581, 591, 638
FD9[b]	0.030	0.001	494/508, 518, 528
FD10[b]	0.044	0.003	553/565, 580, 620

[a] Spectra measured in DMSO. [b] Spectra measured in PBS.

These derivatives differ in the glycoside part, in which the third digitoxose is replaced by a spacer and fluorescent moiety. This modification not only enables monitoring of the compounds but also alters their lipophilicity, thus, affecting their distribution in fluids and tissues.

Therefore, in this part of our study, we aimed to determine whether the newly designed **Dg** derivatives could also bind to NKA. As shown in Fig. S17 and S18, compounds **FD1**, **FD2**, **FD3**, **FD4**, **FD5**, and **FD7** were able to dock into NKA (7WYZ) with their steroid skeleton oriented inwards, and with similar orientation of the steroid skeleton as **Dg**, enabling interaction with Thr_{797}. These compounds exhibited the lowest docking scores among the tested ligands (Table 3).

In contrast, the other four ligands – **FD9**, **FD6**, **FD10** (isomer 5), and **FD8** – docked into NKA with their steroid skeleton rotated, which prevented interaction with Thr_{797} (Fig. S19). As for the derivatized parts of the **Dg** molecules, they were mostly exposed to the solvent, though some interactions, mostly hydrogen bonds, were also present. Notably, **FD10** (isomer 6) failed to dock altogether.

The **Dg** derivative with the lowest docking score (Table 3) was **FD1**, which formed three hydrogen bonds with NKA. The first bond involved the highly conserved hydroxyl group at the C-14 position in the β position of the steroid skeleton, interacting with Thr_{797}. The second bond was between Arg_{880} and the oxygen atom in the second glycosidic bond. The third bond occurred between Glu_{81} (in the β subunit) and the nitrogen atom in the spacer. Notably, the first two hydrogen interactions were also present in the NKA complex with docked **Dg**, highlighting their importance for NKA binding. The next five ligands, namely **FD3**, **FD5**, **FD2**, **FD4**, and **FD7**, also formed hydrogen bonds between the C-14 hydroxyl group and Thr_{797}. Except for **FD4**, these ligands also formed hydrogen bonds with Arg_{880}, similar to **FD1** and **Dg**. In case of **FD7**, a cation-π interaction was present instead of the hydrogen bond. Additionally, **FD3** and **FD2** formed hydrogen bonds between the hydroxyl group on the second digitoxose and Glu_{312} and Glu_{115}, respectively. **FD2** also formed two more hydrogen bonds with Arg_{880} and Asp_{116}, as well as a cation–π interaction with Lys_{79} (in the β subunit). **FD4** exhibited an interaction with Glu_{115}, while **FD7**, in addition to the previously mentioned

Table 3 Binding energies of digitoxin (**Dg**) and its fluorescent derivatives docked into Na^+/K^+-ATPase

Ligand	Binding energies [kcal mol^{-1}]
Dg	−10.172
FD1	−10.227
FD3	−7.876
FD5	−7.436
FD2	−7.287
FD4	−6.526
FD7	−5.067
FD10[a]	−4.895
FD6	−3.384
FD9	−2.942
FD8	1.218

[a] Isomer 5, **F1** – blue BODIPY, **F2** – green BODIPY, **F3** – yellow BODIPY, **F4** – red BODIPY, **F5** – coumarin, **F9** – fluorescein isothiocyanate, **F7** – fluorescein, **F6** – Nile red, **F8** – rhodamine, **F10** – 5(6)-carboxytetramethylrhodamine.

interactions, formed two additional hydrogen bonds: one between Glu_{312} and the first digitoxose, and another between Asn_{790} and the **F7** fluorophore.

In contrast, **FD9** formed a hydrogen bond between the C-14 hydroxyl group and Asn_{122}, and between Arg_{972} and the second glycosidic bond. The remaining ligands – **FD10** (isomer 5), **FD6**, and **FD8** – did not form hydrogen bonds at the C-14 hydroxyl group, likely due to either shallower or deeper binding in the NKA pocket. Nonetheless, **FD10** (isomer 5) formed with NKA three hydrogen bonds: one between the first digitoxose and Glu_{115}, and two more between the oxygen and nitrogen atoms in the spacer and Arg_{882}. **FD6** also formed three hydrogen bonds, however, with different amino acids: one with Asp_{126} and another with Lys_{82} (in the β subunit), involving the first digitoxose and the spacer, respectively. Additionally, a π–π interaction occurred between the **F6** fluorophore and Trp_{887}. The least successfully docked ligand into NKA, was **FD8**, which on one side, formed also at least three interactions with Asp_{121}, Asp_{885}, and Trp_{887}, but on the other, it was docked deeper into the binding NKA pocket resulting in a much higher docking score compared to other ligands, indicating that this deeper binding was energetically less favorable.

In summary, replacing the third digitoxose in **Dg** with a much larger fluorophore moiety altered the position of the steroid skeleton of **Dg** across the set of the evaluated ligands, likely due to variations in spacer length. **FD9** and **FD10** (both isomers) were particularly affected, possibly because their structures contain a polyethylene glycol spacer. However, it is important to note that molecular docking does not account for physicochemical properties such as compound solubility, which is why we focused in our follow-up experiments on the *in vitro* activity of these compounds, including cytotoxicity, intracellular localization, and cell death induction.

2.3 Accumulation and intracellular localization of Dg conjugates

The fluorescent properties of **Dg** derivatives enabled us to study their intracellular accumulation and localization in A549 and MRC-5 cells. This analysis provided valuable insights into their mechanism of action and their ability to cross biological membranes. First, we measured the accumulation of **Dg** derivatives and their respective fluorophores using flow cytometry. The ratios of fluorescence emission intensities of the **Dg** derivatives to their respective fluorophores (Table 4) indicated that the rate of the **FD1**, **FD5**, **FD9**, **FD7**, **FD8**, and **FD10** accumulation in A549 cells was approximately 4–22 times higher compared to the fluorophores (with ratios > 1).

In contrast, **FD2**, **FD3**, **FD4**, and **FD6** accumulated in A549 cells to a lesser extent than their respective fluorophores (with ratios < 1), likely due to their lipophilic nature (Table 4). The only notable exception was **FD7**, which had a similar predicted lipophilicity to that of **FD6**, yet, displayed fluorescence emission intensity ratios (relative to **F7** and **F6**) of 12.8 ± 1.8 and 0.2 ± 0.1, respectively. This is probably because **F7** contains ethyl ester group which can be easily hydrolyzed in aqueous media over time, which results in decreased lipophilicity of its **Dg** conjugate.

Next, we aimed to determine the intracellular localization of all **Dg** derivatives and their corresponding fluorophores in A549 (**FD1–10**: Fig. S20) and MRC-5 cells using live-cell fluorescence microscopy. The microscopic images revealed that the attached fluorophores modulate the intracellular localization of the compounds. Their quantitative colocalization coefficients (QCC) are summarized in Table S1.

Distinct intracellular localization patterns were observed for the investigated **Dg**–fluorophore conjugates in both A549 and MRC-5 cell lines (Fig. 2, 3 and S21–S33). **FD9** and **FD10** predominantly accumulated at plasma membrane (QCC: 0.71 ± 0.08 in A549 cells) and in ER (QCC: 0.79 ± 0.05 in A549 cells), respectively; however, both compounds also showed pronounced localization in lysosomes (QCC: 0.66 ± 0.03 for **FD9** and 0.58 ± 0.07 for **FD10** in A549 cells, Fig. 2, 3 and S21). These results indicate that **FD9** and **FD10** interact with multiple cellular compartments, suggesting a broader intracellular distribution than lysosomal confinement alone. By comparison, **FD1** and **FD5** displayed a distinct localization profile, being primarily localized in lysosomes (QCC: 0.71 ± 0.05 for **FD1** and 0.73 ± 0.03 for **FD5**) and to lower extent in ER (QCC: 0.49 ± 0.10 for **FD1** and 0.47 ± 0.04 for **FD5**, Fig. S23 and S24). On the other hand fluorophores **F1**, **F5**, **F7**, **F9**, **F10** localized in the cells to lower extent compared to the corresponding conjugates as documented in Table 4 and Fig. S34.

Compounds **FD2**, **FD3**, **FD4**, **FD6**, and **FD7** localized in ER (QCC: 0.81 ± 0.03, 0.75 ± 0.08, 0.75 ± 0.05, 0.73 ± 0.01, 0.79 ± 0.01, respectively) and in lysosomes roughly to the same extent (Fig. S25–32, respectively). In these cases, the corresponding fluorophores also showed intracellular localization, either in lysosomes (**F2**, **F3**, **F4**, **F6**; QCC: 0.21 ± 0.42, 0.76 ± 0.01, 0.48 ± 0.25, 0.62 ± 0.02, respectively; Fig. S27 and S30–32) or in the ER (**F3**, **F6**; QCC: 0.76 ± 0.03, 0.80 ± 0.01, respectively; Fig. S26, S28, S29 and S32). Notably, **F2** localized to the ER only in MRC-5 cells (QCC: 0.82 ± 0.04); in A549, its fluorescence pattern suggested predominant accumulation in lipid droplets likely due to its lipophilic character. We believe, for the same reason, that **F4** also partially localized to lipid droplets (Fig. S30). The **FD8**

Table 4 Ratio of fluorescence emission intensities of **Dg** derivatives to their respective fluorophores accumulated in A549 cells growing in a monolayer after 3-h treatment, and their partition coefficients (*C* log *P*, BioByte Corp.).[43] FEIR – fluorescence emission intensity ratio of conjugate and its respective fluorophore. The FEIR values were calculated based on three independent experiments (means with the standard errors of the means; $n = 3$), *C* log *P* values were calculated in ChemDraw Professional 17

Compound	FEIR	*C* log *P*	Compound	*C* log *P*
FD1	19.154 ± 3.117	5.47	**F1**	1.90
FD2	0.302 ± 0.101	9.40	**F2**	5.79
FD3	0.019 ± 0.001	11.13	**F3**	7.51
FD4	0.058 ± 0.007	11.96	**F4**	8.34
FD5	14.933 ± 1.444	6.31	**F5**	2.63
FD6	0.236 ± 0.065	8.58	**F6**	5.10
FD7	12.760 ± 1.798	8.82	**F7**	5.34
FD8	3.245 ± 0.095	5.97	**F8**	2.07
FD9	4.584 ± 0.482	3.20	**F9**	1.89
FD10	20.627 ± 7.773	−0.65	**F10**	−4.24

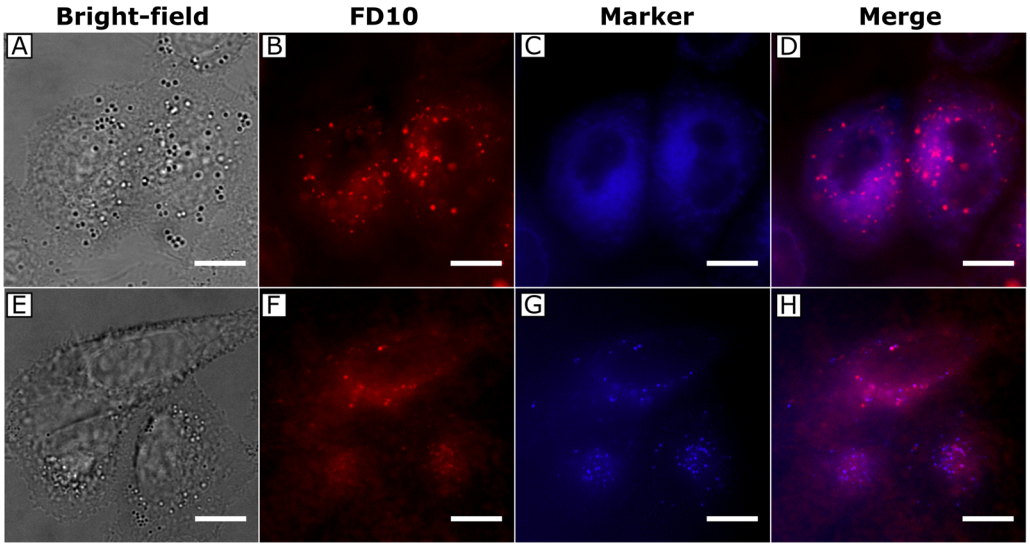

Fig. 2 Fluorescence microscopy images of digitoxin conjugated with 5(6)-carboxytetramethylrhodamine conjugate (**FD10**) and its colocalization with organelle markers in A549 cells. The cells were incubated with **FD10** (0.5 μM) for 4 h and then either with ER-Tracker™ Blue–White (150 nM, 60 min) or with **FD10** with LysoTracker™ Blue DND-22 (70–100 nM, 30–60 min). (A and E) Bright-field images; (B and F), **F10**; (C) ER-Tracker™; (G) LysoTracker™; (D and H) merge. The scale bars represent 10 μm.

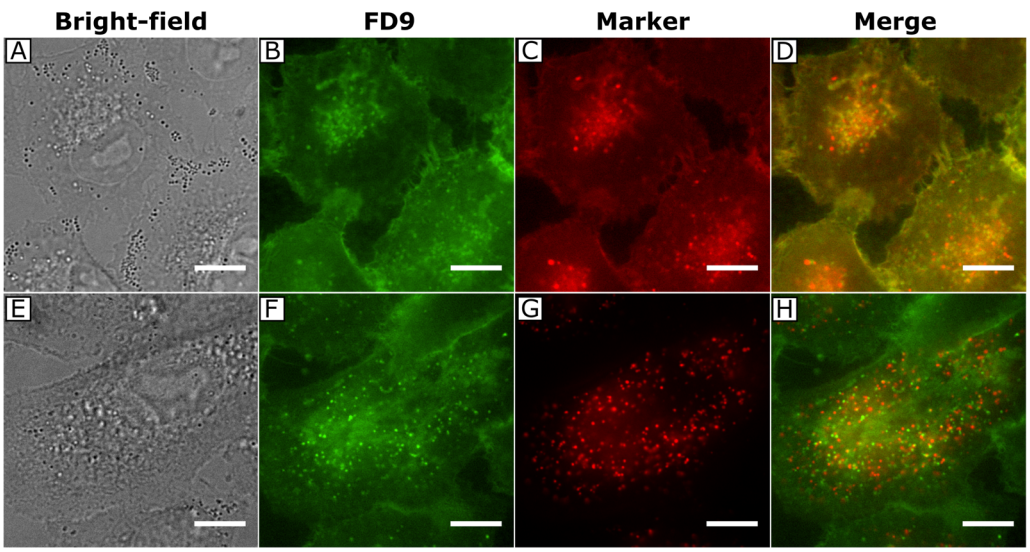

Fig. 3 Fluorescence microscopy images of digitoxin conjugated with 5(6)-carboxytetramethylrhodamine conjugate (**FD9**) and its colocalization with organelle markers in A549 cells. The cells were incubated with **FD9** (0.5 μM) for 5 h and then either with CellMask™ DeepRed (500 μg per μL, 10 min.) or with LysoTracker™ Red DND-99 (70–100 nM, 30 min). (A and E) Bright-field images; (B and F) **FD9**; (C) CellMask™ DeepRed; (G) LysoTracker™, (D and H) merge. The scale bars represent 10 μm.

conjugate and its fluorophore **F8** both localized exclusively to mitochondria (QCC: 0.76 ± 0.03 and 0.75 ± 0.11, respectively), indicating that intracellular distribution in this case was governed primarily by the fluorophore rather than the **Dg** moiety (Fig. S33).

Overall, these results demonstrate that conjugation of **Dg** with fluorophores can significantly alter intracellular distribution. For certain compounds, such as **FD8** and the more lipophilic conjugates **FD2**, **FD3**, and **FD4**, the fluorophore plays a dominant role in determining localization. In contrast, other conjugates, including **FD1**, **FD2**, **FD9**, and **FD10**, exhibited localization patterns distinct from their corresponding fluorophores, with **FD2** showing this difference only in A549 cells.

2.4 Cytotoxicity of Dg derivatives in cell monolayers

Following the intracellular localization studies, we evaluated the cytotoxicity of all compounds (**Dg**, **Dg** derivatives, and fluorophores) in monolayer cultures of A549, MRC-5, and CCRF-CEM cells after 72 h of treatment to assess whether the compounds retained the cytotoxic activity of **Dg**. This

Table 5 Half-maximal inhibitory concentrations (IC_{50}) of digitoxin (**Dg**) and its fluorescent derivatives in A549, MRC-5, and CCRF-CEM cell lines after 72 h of incubation. The IC_{50} values are expressed as the means with the standard errors of the means (SEMs) of at least three independent experiments ($n \geq 3$)[a]

$IC_{50} \pm$ SEM [nM]			
	Cell line		
Compound	A549	MRC-5	CCRF-CEM
Dg	31.59 ± 1.98	45.01 ± 7.07	20 ± 3.5
FD1	346.15 ± 52.58	271.53 ± 37.33	470 ± 70
FD2	467.63 ± 22.85	369.18 ± 32.15	370 ± 120
FD3	399.23 ± 5.34	302.10 ± 22.99	370 ± 99
FD4	580.90 ± 53.35	395.83 ± 52.36	530 ± 78
FD5	491.35 ± 27.17	256.51 ± 21.29	490 ± 40
FD6	1547.75 ± 89.98	882.03 ± 73.02	730 ± 110
FD7	357.48 ± 43.18	245.42 ± 40.95	280 ± 27
FD8	263.05 ± 18.76	377.06 ± 64.16	34 ± 9.2
FD9	294.97 ± 29.05	208.90 ± 37.41	400 ± 57
FD10	169.20 ± 15.30	134.56 ± 10.53	310 ± 49

[a] **F1** – blue BODIPY, **F2** – green BODIPY, **F3** – yellow BODIPY, **F4** – red BODIPY, **F5** – coumarin, **F9** – fluorescein isothiocyanate, **F7** – fluorescein, **F6** – Nile red, **F8** – rhodamine, **F10** – 5(6)-carboxytetramethylrhodamine.

cytotoxicity was quantified by determining IC_{50} values (Table 5). A549 cells were selected because they originate from non-small cell lung cancer, which is generally highly sensitive to CGs.[22]

Among the tested derivatives, **FD10** (the TAMRA conjugated derivative) exhibited the highest cytotoxicity in both A549 and MRC-5 cells, with IC_{50} values of 169.2 ± 15.3 and 134.56 ± 10.53 nM, respectively, whereas its fluorophore was not cytotoxic even at the highest tested concentration (10 μM). In A549 cells, the second most potent derivatives were **FD8** and **FD9**. The aforementioned, **FD9**, exhibited IC_{50} = 263.05 ± 18.76 nM in A549 cells, while its activity in MRC-5 cells was slightly lower (377.06 ± 64.16 nM). Notably, the corresponding fluorophore (**F8**) also displayed some cytotoxicity in A549 cells (IC_{50} = 2.78 ± 0.85 μM after 72 h), for which the **FD8** was excluded from further evaluation. **FD9** (the fluorescein isothiocyanate conjugate) showed cytotoxicity with IC_{50} values of 294.97 ± 29.05 nM in A549 cells and 208.9 ± 37.41 in MRC-5 cells, corresponding to approximately 50–60% lower potency compared to **FD10**. Moreover, fluorophore **F9** was not cytotoxic in the whole range of tested concentrations (up to 10 μM).

A comparable level of cytotoxicity was observed for **FD1** (derivative with blue BODIPY), **FD7** (with fluorescein), and **FD3** (with yellow BODIPY), which displayed closely clustered IC_{50} values in A549 cells (346.15 ± 52.58, 357.48 ± 43.18, and 399.23 ± 5.34 nM, respectively) as well as in MRC-5 cells (271.53 ± 37.33, 245.42 ± 40.95, and 302.10 ± 22.99 nM, respectively).

Lower cytotoxicity was observed for **FD2** and **FD5**, which exhibited IC_{50} values of 467.63 ± 22.85 and 491.35 ± 27.17 nM, respectively, in A549 cells and 369.18 ± 32.15 and 256.51 ± 21.29 nM, respectively, in MRC-5 cells. **FD4** showed further reduced cytotoxicity with IC_{50} of 580.90 ± 53.35 in A549 cells and 395.83 ± 52.36 nM in MRC-5 cells. The least cytotoxic derivative was **FD6**, which exhibited substantially higher IC_{50} values than all other derivatives (1547.75 ± 89.98 nM in A549 and 882.03 ± 73.02 nM in MRC-5 cells), therefore we excluded it from further evaluation.

In CCRF-CEM (Table 5), the cytotoxicity of the **Dg** conjugates ranked from highest to lowest as follows: **FD8** > **FD7** > **FD2** > **FD3** > **DF9** > **FD1** > **FD5** > **FD4** > **FD6**. Overall, their cytotoxic activities were observed in the high nanomolar to micromolar range. A comparable cytotoxicity range was also observed across the other tested cell lines including CEM-DNR, K562, K562-TAX, HCT116, HCT116p53−/−, U-2 OS, and BJ (Tables S2 and S3).

2.5 Cytotoxicity of Dg conjugates in cancer cell spheroids

Based on the promising results obtained from 2D cytotoxicity assays and intracellular localization studies of **Dg** derivatives, we next evaluated their activity in a more physiologically relevant 3D cancer model. Multicellular tumor spheroids more closely recapitulate *in vivo* tumor architecture by reproducing 3D cell organization, cell–cell interactions, and tumor heterogeneity. Importantly, spheroids better stimulate key aspects of the tumor microenvironment, including oxygen and nutrient gradients as well as limited drug penetration, thereby providing a more stringent model for assessing compound efficacy.

To this end, A549-derived spheroids were generated and treated with **Dg** conjugates. Changes in spheroid area and compactness were monitored over a 17-days period. After 3 days treatment, most derivatives induced a marked increase in spheroid area, likely reflecting weakening of intercellular adhesion and reduced structural integrity. Although spheroids remained macroscopically intact at this stage, their compactness was frequently diminished. In contrast, prolonged exposure (17 days) resulted in pronounced disruption of cell–cell interactions, leading to substantial reductions in both spheroid compactness and overall structural integrity, ultimately culminating in spheroid disintegration.

Among all derivatives, **FD10** exhibited the most pronounced early effect (Fig. 4). After 3 days at 10 μM, spheroid compactness decreased to 0.50 ± 0.04 fold relative to the negative control (Fig. S44), accompanied by a 2.58 ± 0.18 fold increase in spheroid area *vs.* control (Fig. S45). Notably, **FD10** induced complete spheroid disintegration by day 6 at concentrations ≥5 μM. In contrast, its corresponding fluorophore **F10** did not significantly affect spheroid area or compactness at any tested concentration, confirming that the observed activity was attributable to the conjugated derivative.

FD9 and **FD7** also demonstrated strong activity. After 3 days, **FD9** (25 μM) and **FD7** (10 μM) induced an increase in A549 spheroid area by 2.93 ± 0.41-fold and 2.74 ± 0.10-fold, respectively, compared to untreated control (Fig. S35 and S36). A significant decrease in compactness together with an increase in spheroid area was observed for **FD9** from 5 μM onward after 3 days of treatment (Fig. S35). Both derivatives induced complete spheroid disintegration by day 6 at concentrations ≥10 μM. Importantly, fluorophore **F9** did not alter spheroid morphology even after 17 days, whereas, **F7** caused only partial

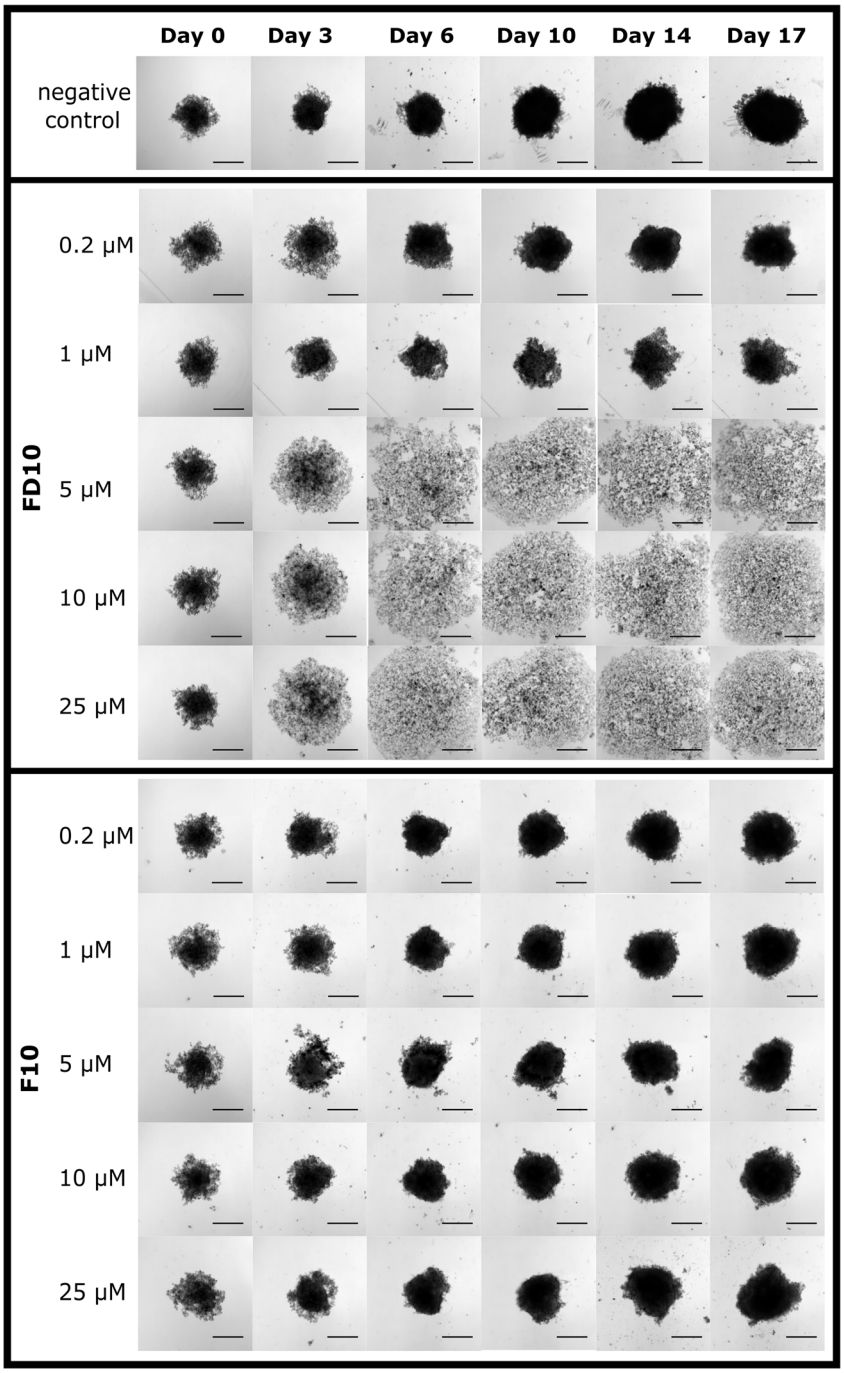

Fig. 4 Bright-field microscopy images of lung adenocarcinoma (A549) cell spheroids treated (day 0) with digitoxin (**Dg**) conjugated to 5(6)-carboxytetramethylrhodamine (**FD10**), **F10** fluorophore or cell culture medium (negative control). Representative images of three independent experiments ($n = 3$) were selected. The scale bars represent 500 μm.

disintegration at 25 μM (compactness reduced to 0.64 ± 0.11 fold relative to control).

Next, **FD3** (10 μM) and **FD2** (25 μM) [Fig. S37 and S38] also induced an increase in spheroid area after 3 days by 2.60 ± 0.23 and 2.59 ± 0.33, respectively. Interestingly, in these cases, area expansion was not accompanied by decreased spheroid compactness, suggesting a distinct morphological response. Nevertheless, **FD3** led to complete spheroid disintegration by day 10 at concentrations ≥5 μM. The fluorophore **F2** induced partial spheroid disintegration only at the highest tested concentration (25 μM).

The remaining derivatives – **FD1**, **FD4**, **FD5** (Fig. S39–S41) – induced the highest increase in spheroid area compared to the negative control. After 3 days, **FD1** and **FD4** at 10 μM increased spheroid area by 1.58 ± 0.16 and 2.04 ± 0.14 fold, respectively, while **FD5** at 25 μM induced a 1.66 ± 0.24 fold increase.

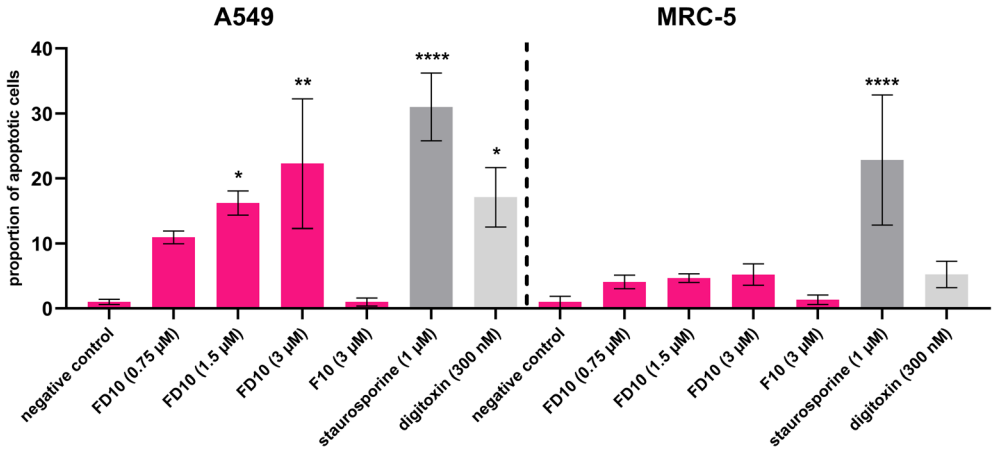

Fig. 5 Concentration-dependent induction of apoptosis in A549 and MRC-5 cells growing in a cell monolayer by digitoxin (**Dg**), its derivative **FD10** and fluorophore **F10** after 48-h treatment at several concentrations. The values represent the means ± the standard deviations of normalized data calculated from three independent experiments and are expressed as folds of the negative control (cells treated only with cell culture media). As a positive control, 1-μM staurosporine was used. The number of * represents the degree of significance (One-Way Analysis of Variance) compared to the negative control. *$p < 0.05$, **$p < 0.01$, and ****$p < 0.0001$; $n = 3$.

However, these changes were not associated with significant reductions in compactness under these conditions. Their respective fluorophores **F1**, **F4**, and **F5** did not induce detectable morphological changes in the A549 cell spheroids at any concentration throughout the 17-days incubation period. The parent compound **Dg** (Fig. S42), used as a positive control, induced morphological changes at concentrations as low as 200 nM. The most pronounced increase in area was observed at 10 μM, resulting in 2.56 ± 0.63 fold increase in spheroid area and a reduction in compactness to 0.51 ± 0.09 relative to negative control.

Overall, all derivatives induced at least partial spheroid disintegration after 3 days at concentrations ≥5 μM (Fig. S43), with the exception of **FD9** which caused partial disintegration already at 1 μM. At lower concentrations, the derivatives primarily decreased the rate of spheroid area increase without causing disintegration (by roughly 20–30%). After 17 days, almost all derivatives (except **FD1** and **FD3**) and **Dg** caused near-complete spheroid disintegration at concentrations ≥5 μM (Fig. S46 and S47). In summary, **FD10** and **FD9** emerged as the most potent derivatives in disintegration of A549 spheroids. **FD10** achieved a degree of spheroid disintegration comparable to **Dg** at concentrations ≥5 μM, while **FD9** induced partial disintegration already at 1 μM after 17 days. Crucially, the corresponding fluorophores did not significantly affect spheroid morphology, confirming that the observed activity derives from the **Dg** conjugates rather than the fluorophore moieties.

2.6 Apoptosis induction analysis

Since apoptosis is a predominant mode of cell death induced by **Dg**, we investigated whether the **Dg** derivatives **FD9** and **FD10** retained this ability. Both conjugates exhibited good cytotoxicity in multicellular spheroids and displayed intracellular localization patterns distinct from their corresponding fluorophores. Apoptosis induction was assessed by flow cytometry using fluorescent annexin V staining of externalized phosphatidylserine. To avoid spectral overlap, green-emitting annexin was used for **FD10** analysis, whereas blue-emitting annexin was used for **FD9**.

Preliminary experiments showed that **Dg** induced a stronger apoptotic response in A549 cells after 48 h compared to 24 h of treatment. Based on these results, apoptosis induction by **F10** and **F9** was evaluated exclusively after 48 h. To compare responses in cancerous and non-cancerous cells, both A549 and MRC-5 cell lines were treated with **FD10** (0.75–3 μM) or **FD9** (2.5–10 μM).

In A549 cells, both **FD10** and **FD9** induced apoptosis in a significantly higher proportion of cells compared to the negative control (**FD10**: 16.2 ± 1.9 with $p < 0.05$, and 22.3 ± 10.0 with $p < 0.01$, respectively, Fig. 5, and **FD9**: 24.7 ± 11.2 with $p < 0.05$, and 41.9 ± 13.4 with $p < 0.001$, respectively, Fig. S48, values are fold of negative control). In contrast, the corresponding fluorophores **F10** and **F9** did not induce apoptosis and were not significantly different from the negative control (1.0 ± 0.6 and 1.0 ± 0.1, respectively, values are fold of negative control), indicating that apoptosis induction was attributable to the **Dg** moiety. As expected, the positive control staurosporine and **Dg** induced significantly higher levels of apoptosis compared to the negative control for both annexin probes ($p < 0.05$ and $p < 0.0001$ for green- and blue-emitting annexin, respectively).

In the non-cancerous MRC-5 cell line, a significant increase in apoptotic cells was observed only for staurosporine (green-emitting annexin: 22.8 ± 10 with $p < 0.0001$; blue-emitting annexin: 27.5 ± 7.1 with $p < 0.05$, values are fold of negative control) compared to negative control, whereas **FD9**, **FD10**, their fluorophores, or Dg did not induce significant changes (Fig. 5 and S48). Overall, these results demonstrate that **FD9** and **FD10** effectively induce apoptosis in A549 cancer cells, with minimal effects in non-cancerous MRC-5 cells, and confirm that the observed apoptotic activity is driven by the **Dg** moiety rather than the fluorophore.

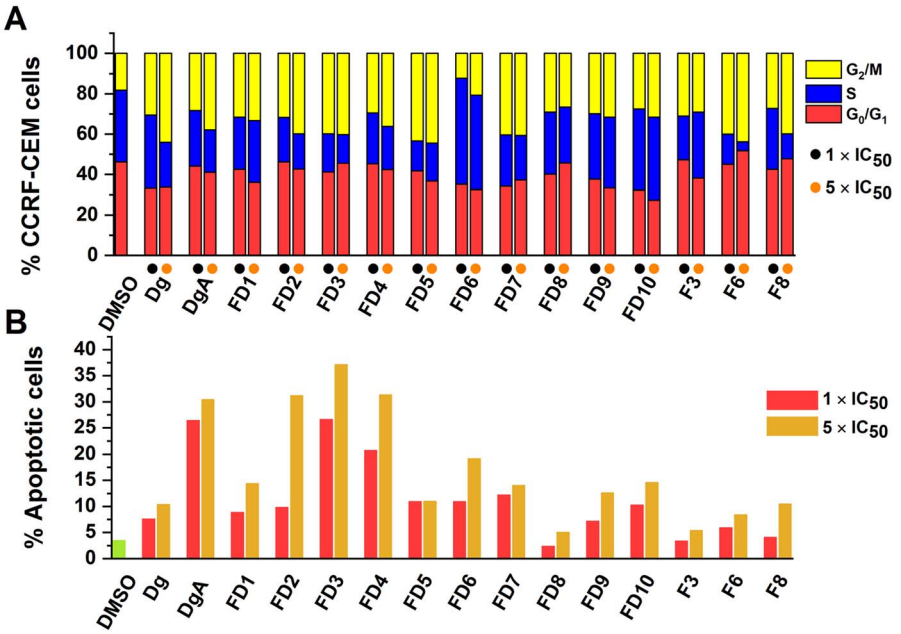

Fig. 6 Cytotoxic effect of compounds on cell cycle and apoptosis in CCRF-CEM lymphoblasts (% of positive cells). Flow cytometry analysis was used for the quantification of cell cycle distribution (A) and apoptosis (B) with a concentration equal to 1 × IC_{50} and 5 × IC_{50}. The sum of the percentages for the G_0/G_1, S, and G_2/M is equal to 100%. The table with values is shown in Table S4 in SI.

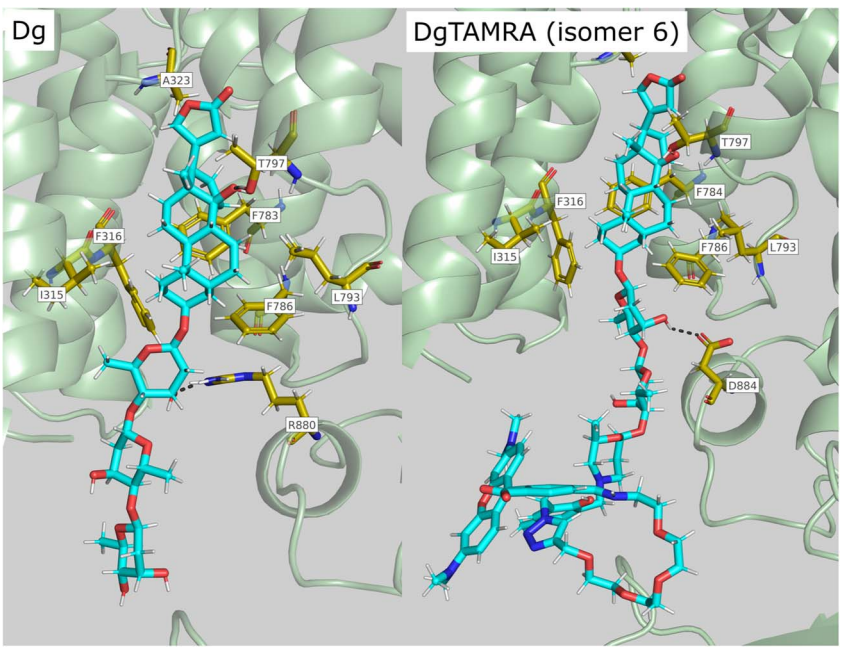

Fig. 7 3D visualization of Na^+/K^+-ATPase binding pocket (7WYZ, conformation E2P, organism: *Squalus acanthias*, acquired from Protein Data Bank) in complex with **Dg** or **FD10** (isomer 6) after 100 ns molecular dynamics simulation. Hydrogen bonds between ligands and amino acids are depicted with dashed black line. Helix M_2 was removed.

2.7 Cell cycle and cell death analysis in leukemic lymphoblasts

Flow cytometry of CCRF-CEM lymphoblasts exposed to **Dg** and its derivatives (Table S4 and Fig. 6) revealed a reproducible low-dose shift from the S phase to the G_2/M across multiple **Dg** conjugates, with the same trend detectable for **Dg** itself. This redistribution became more prominent at higher concentrations, at which several derivatives reached the G_2/M fractions of ~40%. The sub-G_1 increased for several **Dg** derivatives (notably **DgA**, **FD2–FD4**), rising up to ~30–37% at 5 × IC_{50}—which is

a pattern typical for apoptotic DNA fragmentation and cytotoxic activity rather than cell-cycle arrest. Taken together, these data indicate that the dominant response is apoptosis, while the G_2/M elevation, particularly at higher doses, most likely reflects a secondary consequence of cytotoxic stress preceding cell death rather than a specific checkpoint block. This interpretation is consistent with the Annexin-V/PI data in A549 cells. Under these conditions, the **Dg** derivatives primarily trigger programmed cell death rather than a canonical cell-cycle block.

2.8 Molecular dynamics simulations

Our *in vitro* experiments demonstrated that **FD10** and **FD9** were the best performing derivatives in terms of their cytotoxicity and intracellular localization. However, there was a clear distinction when compared with the molecular docking data, as both derivatives exhibited different docking patterns compared to **Dg**. To gain further insights into their binding mechanisms, we conducted 100 ns long molecular dynamics simulations of each NKA-ligand complex solvated in water. The length of 100 ns was chosen as it is less computationally demanding and provides sufficient data to reliably analyze the behavior of NKA-ligand complex. After a 100 ns simulation, all ligands remained stable in the NKA binding pocket, although not all of them formed a hydrogen bond with Thr_{797}. Among the four ligands tested [**Dg**, **FD10** (isomers 5 and 6), and **FD9**], **Dg** and **FD10** (isomer 6) formed a hydrogen bond *via* the hydroxyl group at the C-14 position (Fig. 7). Additionally, **Dg** and **FD10** (isomer 6) established hydrogen bonds through the first digitoxose with Arg_{880} and Asp_{884}, respectively. In contrast, **FD10** (isomer 5) and **FD9** did not form these bonds (Fig. S49). Instead, the steroid skeleton of these two ligands was likely stabilized in the binding pocket through hydrophobic interactions with Phe_{783} and Ile_{320}. Moreover, the fluorophore region of **FD9** formed hydrogen bonds with Asp_{121}, Arg_{880}, and Asp_{884}. These interactions may explain why the conformation of the steroid skeleton in the NKA binding pocket differed from that of **Dg**. In contrast, no such interactions were present in the NKA complex with **FD10** (isomer 5) [Fig. S49].

3 Discussion

Dg is a potent inhibitor of NKA, exhibiting strong cytotoxic effects against various cancer cell lines, as demonstrated in numerous studies.[17–22] To better understand **Dg**'s mechanism of action, it is beneficial to monitor it directly in biological system, however, **Dg** itself cannot be directly tracked. Therefore, conjugating **Dg** with a traceable tag could be advantageous, making it useful not only in cancer therapy but also in diagnostics. To this end, we designed, synthesized and evaluated the biological activity of 10 novel **Dg** derivatives. The fluorescent tags chosen for this synthesis were selected based on their widespread use in biochemical research. The varying chemical structures of these tags can alter the intracellular distribution as well as solubility of the derivatives, primarily due to differences in the hydrophilicity and molecular weight. Therefore, in this study, we evaluated the derivatives' binding to NKA, their cytotoxicity in cell monolayers, in cancer cell spheroids, their intracellular localization, and also the ability to induce cell death by apoptosis.

To investigate the binding of **Dg** derivatives to NKA, we first employed molecular docking. Successful binding of CGs to NKA relies mainly on their interaction with Thr_{797}, which forms a hydrogen bond with the conserved hydroxyl group at the C-14 in the β position.[50] This interaction was observed for **FD1**, **FD2**, **FD3**, **FD4**, **FD5**, and **FD7**. These derivatives also displayed a similar orientation of their steroid skeletons within the binding pocket of NKA, comparable to that of **Dg** and ouabain as observed in X-ray crystal structures[50,51] and cryo-electron microscopy data.[52] In contrast, this binding mode was not observed for **FD9** and **FD10** (isomer 5). Specifically, **FD9** formed a hydrogen bond between its C-14 hydroxyl group and Asn_{122}, rather than with Thr_{797}. **FD10** (isomer 5) did not form a hydrogen bond *via* the C-14 hydroxyl group at all, while **FD10** (isomer 6) failed to dock into the binding pocket entirely. However, it is important to note that molecular docking can sometimes fail to predict ligand conformation consistent with those determined by experimental methods such as X-ray crystallography or cryo-electron microscopy.[52] Therefore, we subsequently employed molecular dynamics simulations to further investigate these interactions.

Despite these findings, we shifted our focus to the intracellular localization and cytotoxicity of the **Dg** derivatives in A549 and MRC-5 cell monolayers. Among all tested compounds, **FD10** and **FD9** emerged as the best-performing derivatives. Overall, they both retained the cytotoxicity of **Dg** to the highest extent in all tested cell lines, with the lowest IC_{50} values being in A549 cells (169.2 ± 15.3 and 294.97 ± 29.05 nM, respectively). We attribute this to their hydrophilicity which closely resembles that of **Dg**. This enhanced hydrophilicity likely contributes to better solubility in cell culture media, improving their availability for NKA inhibition. Also **FD10** and **FD9** exhibited significantly higher ($p < 0.05$ and < 0.01, respectively) cytotoxicity in A549 compared to CCRF-CEM cells which is probably due to the in general higher NKA expression in lung cancer cells compared to lymphoma.[53] Moreover, consistent with reported data, that extending the side chain at the C-3 position reduces cytotoxicity across various cell lines, including lung cancer cells,[22] all derivatives exhibited higher IC_{50} values compared to **Dg** (Table 4). Nonetheless, considering reported dose-limiting systemic toxicity of **Dg**, this reduction is viewed as an acceptable trade-off.

Following cytotoxicity studies in cell monolayers, we proceeded to investigate the intracellular localization of **Dg** derivatives in these monolayers. **FD10** preferentially localized in lysosomes and ER whereas **FD9** was predominantly found at the cytoplasmic membrane and also in lysosomes. Notably, the accumulation of free fluorophores (**F10** and **F9**) in A549 cells was significantly lower, 20.6 ± 7.8 and 4.6 ± 0.5 times less, respectively, compared to its conjugates – indicating that the observed intracellular distribution of the conjugates was driven primarily by the **Dg** moiety. This observation correlates well with their low $C\log P$ values, the lowest among all tested compounds (Table 5). The lysosomal localization of both **FD10**

and **FD9** is consistent with NKA internalization and its intracellular trafficking upon its inhibition, as previously reported for ouabain in ref. 54. Additionally, the ER localization of **FD10** suggests that beyond receptor-mediated internalization, passive diffusion also occurs, enabling binding to newly synthesized NKA prior to its transport to the plasma membrane. This is consistent with the fact that NKA can only be transported to the cytoplasmic membrane if it is in its dimeric form with β subunit.[55] Meanwhile, **FD9**'s localization at the cytoplasmic membrane indicates direct interaction with membrane-bound NKA at its site of action.

In A549 cell spheroids, which are far more complex than cell monolayers, **FD10** exhibited the greatest reduction in compactness at concentration of 10 μM (0.50 ± 0.04 times the negative control) while **FD9** showed similar effect at 25 μM (0.52 ± 0.03 times the negative control) and at the same time, there was an increase in the spheroid area: 2.58 ± 0.18 and 2.49 ± 0.38 times the negative control, respectively. Notably, these effects are comparable to those observed with the positive control, **Dg**, at 10 μM concentration, which resulted in area increase of 2.56 ± 0.63 times the negative control and compactness 0.51 ± 0.09 times the negative control. Both parameters – the decreased compactness and increased area – are indicative of reduced cell viability in the spheroids. Similar outcomes were reported in ref. 56 and 57, in which lung cancer cell (H460) spheroids treated with digitoxigenin derivatives (aglycones of **Dg**) showed approximately a 50% reduction in spheroid area after a 3-days treatment with C10 and C18 derivatives. In our study, while we also observed reduced compactness and increased area of the spheroids after 3 days, a more significant was the marked reduction in spheroid area after 17 days of treatment. This extended effect suggests that compound penetration into spheroids is closely associated with the hydrophilicity of the derivatives. Specifically, since both C10 and C18 are less hydrophilic than **FD10**, this may explain their delayed but sustained impact on spheroid structure and viability.

FD7 was the third compound to induce a significant increase in spheroid area after three days (2.74 ± 0.10 times the negative control). Notably, this effect was achieved at 10 μM concentration, unlike **FD10** and **FD9**, which required 25 μM concentration. Also, fluorescence imaging showed at least partial intracellular localization of **FD7** in the ER and lysosomes; however, the intensity of fluorescence emission in both organelles was weak despite the compound's high predicted $C\log P$ of 8.82. We attribute this to the presence of an ester group in both **FD7** and its fluorophore **F7**, which might be hydrolyzed during incubation. This hydrolysis would yield a more hydrophilic derivative, reducing the $C\log P$ to 0.59 and 4.06 for **FD7** and **F7**, respectively.

Among the four BODIPY conjugates, only **FD1** demonstrated a higher rate of intracellular accumulation compared to its unconjugated fluorophore (**F1**). Despite this, **FD1** was the least cytotoxic of the **Dg**-BODIPY conjugates, even though all BODIPY derivatives localized in both the ER and lysosomes. These findings suggest that both the intracellular accumulation and the ability of these compounds to induce spheroid disintegration are also influenced by the compound's lipophilicity. It is well established that more hydrophilic compounds penetrate cell spheroids more rapidly than hydrophobic ones. However, over time, both types (hydrophilic and hydrophobic compounds) can reach similar intracellular concentrations, as was shown in ref. 58. Importantly, increased lipophilicity may enhance compound retention within the spheroid, thereby prolonging their cytotoxic effects even under conditions involving frequent media changes. This may explain why only **FD3** and **FD4** induced complete disintegration of A549 cell spheroids after 17 days of treatment at concentrations of 5, 10, and 25 μM. These two compounds have predicted $C\log P$ values of 11.13 and 11.96, respectively, which is approximately 2–6 times higher than those of **FD1** and **FD2**. A similar trend was observed for **FD5** ($C\log P = 6.31$). Taken together, these findings suggest that effective disintegration of A549 cancer cell spheroids by **Dg** conjugates depends on the compound's hydro-/lipophilicity. Specifically, conjugates must be either sufficiently hydrophilic (*e.g.*, **FD10**, **FD9**, and **FD7**) to penetrate inside the A549 cell spheroid rapidly, or sufficiently hydrophobic (*e.g.* **FD3** and **FD4**) to remain within the spheroids long enough to exert sustained cytotoxic effects.

In addition to lipophilicity, another potential explanation for the generally lower cytotoxicity of the tested compounds in A549 cell spheroids compared to monolayer cultures could be the expression of tight junction proteins, such as occludin and claudin. These proteins can suppress drug accumulation within spheroids and thereby enhance resistance to anticancer agents. This has been demonstrated in ref. 59, in which elevated levels of occluding and claudin in A549 cell spheroids were associated with reduced efficacy of cisplatin, doxorubicin, and gemcitabine. Further evidence of occludin role comes from ref. 60, in which the authors reported that knockdown of occludin in lung cancer cells (SPC-A1) resulted in reduced proliferation and increased apoptosis. Similarly, reduced expression of claudin in A549 cell spheroids was shown to increase sensitivity to doxorubicin following 24-h incubation.[61,62]

Based on these findings, we selected **FD10** and **FD9**, our most cytotoxic **Dg** conjugates, which also caused the most extensive A549 cell spheroid disintegration, for apoptosis studies. Apoptosis is highly desirable mechanism of cancer cell death, as it involves the regulated fragmentation of cellular components, thereby minimizing inflammatory responses and damage of surrounding tissues.[63] Consequently, the ability to induce apoptosis is a key criterion in the assessment of potential anticancer drug candidates. **Dg** is known to trigger apoptosis in a variety of human cancer cell lines,[17–20] primarily through inhibition of NKA. This inhibition leads to an increase in intracellular Ca^{2+} levels and activation of the mitochondrial apoptotic pathway.[64,65]

Both **FD10** and **FD9** induced apoptosis in A549 cells after 48 h in a concentration-dependent manner. In contrast, the unconjugated fluorophores (**F10** and **F9**) serving as negative controls, showed minimal apoptotic activity, which was expected due to their reported biocompatibility and low cytotoxicity.[66,67] Given that **Dg** is a good apoptosis inducer,[17–20] and **F10** and **F9** showed no significant apoptotic effect, we can conclude

that these results support the conclusion that the pro-apoptotic effects observed with **FD10** and **FD9** are attributable to the **Dg** moiety, rather than the fluorescent parts of the molecule.

Furthermore, no significant differences were observed in apoptosis induction between **FD10**, **FD9**, and **Dg** treatment at 1.5 μM, 5 μM, and 300 nM concentration, respectively, indicating that all three compounds induced apoptosis to a similar extent. As expected, the level of apoptosis induction in noncancerous MRC-5 cells was significantly lower compared to cancerous A549 cells, consistent with previous findings in primary small airway epithelial cells (pSAEC), as reported in ref. 17. This is probably because MRC-5 as non-cancerous cells are in general less sensitive toward chemotherapy, compared to A549 cells.[68] The only exception was the positive control, staurosporine, which induced high levels of apoptosis in both cell types.

Given the differences between the *in silico* binding affinities and the *in vitro* cytotoxicity results for **FD10** and **FD9**, we conducted molecular dynamics simulations of NKA complexes with **Dg**, **FD10** (both isomers), and **FD9**. In our analysis, we focused on two key aspects: (i) the presence of the hydrogen bond between the C-14 hydroxyl group of the steroid core and Thr_{797}, and (ii) the orientation of the steroid moiety within the NKA binding pocket. This critical hydrogen bond was observed in the **Dg** and **FD10** (isomer 6) complexes, with the steroid skeleton of **FD10** (isomer 6) adopting a similar orientation to that of **Dg**. These findings align with the crystallographic and cryo-electron microscopy data reported by Laursen *et al.*[50,51] and Kanai *et al.*,[52] respectively, who showed that ouabain, a structurally related compound, binds to NKA in the same orientation and depth of its steroids core, and also formed a hydrogen bond between C-14 hydroxyl group and Thr_{797} of NKA.

In contrast, this hydrogen bond was absent in the NKA complexes with **FD10** (isomer 5) and **FD9**, likely due to a slightly different orientation of their steroid skeleton. Interestingly, **FD9** formed hydrogen bonds between its fluorophore moiety and Asp_{121}, Arg_{880}, and Asp_{884} of NKA. In ref. 56, the authors reported that hydrogen bonding at the first saccharide moiety of CGs is crucial for their effective binding into NKA and that bulky substituents on the glycoside region of CGs can disrupt these interactions. In our study, the presence of these key hydrogen bonds in **Dg**- and **FD10** (isomer 6)-NKA complexes, and their absence in **FD10** (isomer 5)- and **FD9**-NKA complexes, likely explains the distinct orientation of their steroid skeletons.

Overall, our data suggest that the biological activity of fluorescent **Dg** conjugates is governed by the combined influence of several structural parameters rather than by a single physicochemical property. In particular, moderate lipophilicity, as observed for **FD9** and **FD10**, appears to facilitate rapid cellular uptake, likely due to improved aqueous solubility, resulting in enhanced cytotoxicity. In contrast, the more lipophilic derivatives, such as **FD3** and **FD4**, exhibited prolonged retention in a three-dimensional cell line spheroid model, leading to sustained cytotoxic effects despite slower initial penetration.

Besides lipophilicity, modifications of the saccharide moiety, including the length and composition of the linker introduced at the C-3 position, also influenced biological activity. These structural changes affect both the physicochemical properties of the conjugates, including their aqueous solubility and bioavailability in cell culture media, and their predicted interactions with Na^+/K^+-ATPase. In particular, molecular dynamics simulations suggested that preservation of the interaction with the key residue Thr_{797} may contribute to maintaining target recognition following fluorophore conjugation.

Intracellular localization studies provided additional insight into the relationship between molecular structure, cellular distribution, and biological activity. The preferential localization of **FD9** at the plasma membrane and **FD10** within the endoplasmic reticulum and lysosomes is consistent with their cellular accessibility to Na^+/K^+-ATPase and with the predicted retention of target-related activity, although direct experimental validation of target engagement remains necessary. Collectively, these findings indicate that **FD9** and **FD10** represent derivatives in which the loss of activity associated with structural modification is minimized while the advantages of fluorescent labeling are retained.

Importantly, fluorophore conjugation of the **Dg** scaffold inherently introduces a biological cost, primarily reflected by reduced cytotoxic potency compared with the parent unmodified compound. This decrease likely results from a combination of steric and physicochemical effects, including increased molecular size, altered lipophilicity, and potential changes in membrane permeability or target accessibility. Therefore, derivatization results in a shift in the activity profile, in which only a subset of the conjugates preserves substantial antiproliferative activity. However, this reduction in potency is accompanied by a valuable functional gain: fluorescence-based intracellular traceability, enabling direct visualization of cellular uptake and intracellular distribution that cannot be achieved with native **Dg**. The retention of significant activity by **FD9** and **FD10** demonstrated that this trade-off is not absolute and highlights the capacity of the **Dg** scaffold to tolerate structural expansion while maintaining relevant biological properties.

4 Conclusion

In summary, we designed, synthesized, and characterized fluorescent derivatives of **Dg** and evaluated their biological activities across several cell lines together with their predicted interactions with Na^+/K^+-ATPase. To the best of our knowledge, this is the first comprehensive study reporting both the synthesis of these novel fluorescent **Dg** derivatives and their biological characterization. Among the compounds tested, **FD10** and **FD9** emerged as the most promising candidates. Molecular dynamic simulations indicated their ability to form stable complexes with Na^+/K^+-ATPase, suggesting that fluorophore conjugation does not preclude interaction with the established molecular target of **Dg**. In biological assays, **FD10** and **FD9** exhibited cytotoxic profiles in A549 cells, growing in a monolayer, that were the closest to that of the parent compound **Dg**. Notably, both derivatives induced pronounced morphological changes in A549 spheroids, including the highest reduction in spheroid compactness and subsequent

spheroid disintegration during prolonged treatment. Furthermore, **FD10** and **FD9** triggered a strong proapoptotic response in A549 cells growing in a monolayer after 48 h of treatment, compared to no effect observed in noncancerous lung fibroblasts MRC-5. In addition to their biological activity, fluorescence microscopy enabled visualization of intracellular localization of the **Dg** derivatives, demonstrating their possible use as fluorescent probes. Overall, these findings identify **FD10** and **FD9** as promising lead structures for further optimization and provide a foundation for future studies aimed at developing **Dg** derivatives with combined anticancer and imaging properties.

5 Materials and methods

5.1 Synthesis of digitoxin derivatives

5.1.1 Chemistry. NMR spectra were recorded by Agilent-MR DDR2 (Varian, Palo Alto, CA, USA). The Quadrupole LC/MS (ESI ionization) with an Infinity III LC system (Agilent Technologies, Santa Clara, USA) was used for LR-MS and HPLC analyses (C18 column: 100 mm; UV detection). Elution with a flowrate of 0.3 mL min^{-1} and the following systems were used: A 50% MeOH, B absolute MeOH (**DgA**: 0–10 min (100% B); all FDs: 0–16 min (100% B), 18 min (50% A, 50% B), 20 min (100% A)). HRMS were measured by LTQ ORBITRAP VELOS with $HESI^+$/$HESI^-$ ionization (Thermo Scientific, Waltham, USA). Absorption and fluorescence spectra were measured in DMSO or PBS using quartz cells of 1 cm path length. Absorption spectra were recorded using Cary 60 spectrophotometer (data interval 0.5 nm, averaging time 0.1 s) and fluorescence spectra were measured using Cary Eclipse fluorescence spectrophotometer equipped with R3896 PMT (data interval 0.5 nm, averaging time 0.1 s, PMT voltage 600 V, effective slits 5 nm or 2.5 nm, excitation filter "Auto", emission filter "Open"). The data were obtained and evaluated using procedures established in our working group.[69]

For thin-layer chromatography (TLC), aluminum silica gel sheets for detection in UV light (TLC silica gel 60 F254, Merck) were used. For TLC visualization, a diluted solution of H_2SO_4 in MeOH was used and plates were heated. For column chromatography, 30–60 μm silica gel (ICN Biomedicals, Costa Mesa, USA) was used.

5.1.2 Chemicals. The following chemicals were purchased from TCI Europe (Zwijndrecht, Belgium): sodium cyanoborohydride – $NaBH_3CN$ (>95%), sodium azide – NaN_3 (>99%), sodium ascorbate (>98%), triphenylphosphine – PPh_3 (>95%), tris[(1-benzyl-1*H*-1,2,3-triazol-4-yl)methyl]amine – TBTA (>97%), piperidine (>99%). Copper(II) sulfate pentahydrate – $CuSO_4 \cdot 5H_2O$ (≥98.0%), sodium periodate – $NaIO_4$ (≥99.8%), 4-(dimethylamino)benzaldehyde (99%), 3-hydroxybenzaldehyde (≥99%) were purchased from Sigma-Aldrich (Prague, Czech Republic). The solvents for column chromatography and reactions were purchased from PENTA (Prague, Czech Republic) and were used as delivered.

5.1.3 Synthesis of BODIPY dyes. To a BODIPY **F2** (350 mg, 1.11 mmol) and 3-hydroxybenzaldehyde (135 mg, 1.59 mmol) or 4-(dimethylamino)benzaldehyde (166 mg, 1.11 mmol) in dry benzene (5 mL) HOAc (100 μL) and piperidine (110 μL) were added and the vial was closed with pressure-cap. The flask was placed onto microwave reactor and stirred for 1 h at 120 °C. The cooled reaction mixture was chromatographed on silica gel column. The products thus obtained were lyophilized from 1,4-dioxane and stored in the fridge at the dark.

5.1.4 3-(3-Hydroxybenzylidene)-8-pent-4-yne BODIPY (F3). Chromatography (2×): hexane-AcOEt 5 : 1 → 3 : 1 (v/v) and cyclohexane-AcOEt 5 : 1 (v/v). The product (42 mg, 0.099 mmol) obtained as dark pink lyophilizate in 9% yield. R_F = 0.3 in cyclohexane-AcOEt 3 : 1 (v/v). ^{1}H NMR (400 MHz, $CDCl_3$) *δ*: 7.59 (dt, *J* = 16.3, 1.8 Hz, 1H), 7.21 (t, *J* = 7.8 Hz, 1H), 7.17–7.08 (m, 2H), 7.06 (t, *J* = 2.0 Hz, 1H), 6.77 (ddd, *J* = 8.0, 2.5, 0.9 Hz, 1H), 6.66 (s, 1H), 6.10 (s, 1H), 5.06 (s, 1H), 3.16–3.07 (m, 2H), 2.57 (s, 3H), 2.49 (s, 3H), 2.46 (s, 3H), 2.41 (td, *J* = 6.6, 2.7 Hz, 2H), 2.06 (t, *J* = 2.6 Hz, 1H), 1.85 (dq, *J* = 11.0, 6.6 Hz, 2H); Fig. S2A. ^{13}C NMR (101 MHz, $CDCl_3$) *δ*: 156.03, 154.70, 151.29, 144.31, 140.72, 139.94, 138.32, 135.22, 132.87, 132.19, 130.03, 122.22, 120.65, 119.59, 118.28, 116.09, 113.45, 82.93, 70.12, 30.14, 27.53, 19.06, 16.93, 16.77, 14.80 (t, $J_{C,F}$ = 2.5 Hz); Fig. S2B. HRMS-ESI: for $C_{25}H_{25}BF_2N_2O$ calcd 418.20280 Da, found *m*/*z* 441.19270 $[M + Na]^+$; Fig. S2C.

5.1.5 3-(4-Dimethylaminobenzylidene)-8-pent-4-yne BODIPY (F4). Chromatography: toluene. The product (68 mg, 0.15 mmol) was obtained dark blue lyophilizate in 14% yield. R_F = 0.25 in cyclohexane-AcOEt 5 : 1 (v/v). ^{1}H NMR (400 MHz, $CDCl_3$) *δ*: 7.52–7.46 (m, 2H), 7.44 (m, 1H overlap with multiplet at 7.52-7.46 ppm), 7.19 (d, *J* = 16.1 Hz, 1H), 6.68 (d, *J* = 11.1 Hz, 3H), 6.04 (s, 1H), 3.13–3.06 (m, 2H), 3.01 (s, 6H), 2.56 (s, 3H), 2.48 (s, 3H), 2.44 (s, 3H), 2.40 (td, *J* = 6.7, 2.7 Hz, 2H), 2.05 (t, *J* = 2.6 Hz, 1H), 1.84 (*p*, *J* = 6.8 Hz, 2H); Fig. S3A. ^{13}C NMR (101 MHz, $CDCl_3$) *δ*: 153.76, 151.89, 150.99, 142.36, 140.57, 138.30, 137.38, 133.17, 131.35, 129.25, 124.84, 121.13, 118.39, 114.53, 112.19, 83.06, 69.96, 40.42, 30.17, 27.38, 19.01, 17.01, 16.57, 14.63 (t, $J_{C,F}$ = 2.5 Hz); Fig. S3B. HRMS-ESI: for $C_{27}H_{30}BF_2N_3$ calcd 445.25008 Da, found *m*/*z* 446.25659 $[M + H]^+$, 468.23995 $[M + Na]^+$; Fig. S3C.

5.1.6 2-(Aminomethyl)-6-(azidomethyl)-4-methylphenol (AP). To a solution of 2,6-bis(azidomethyl)-4-methylphenol (2.5 g, 11.5 mmol) in THF (20 mL) PPh_3 (3.3 g, 12.6 mmol) in THF (20 mL) was added. After the addition of PPh_3 water was added (2.5 mL) and the mixture was stirred overnight at RT. The solids formed were filtered off (diamine), the solvents were removed under reduced pressure and the residue was chromatographed ($CHCl_3$–MeOH 40 : 1 to 15 : 1, v/v). AP (830 mg, 4.3 mmol) was obtained as a beige material in 38% yield. R_F = 0.25 in DCM-MeOH 20 : 1 (v/v); visualization with ninhydrin. ^{1}H NMR (400 MHz, $CDCl_3$) *δ*: 6.96 (d, *J* = 2.2 Hz, 1H), 6.78 (d, *J* = 2.2 Hz, 1H), 5.17 (s, 2H), 4.35 (s, 2H), 4.08 (s, 2H), 2.25 (s, 3H); Fig. S4A. ^{13}C NMR (101 MHz, $CDCl_3$) *δ*: 154.53, 129.60, 128.96, 127.91, 123.83, 122.56, 49.94, 45.31, 20.44; Fig. S4B.

5.1.7 Azidodigitoxin (DgA). To a solution of **Dg** (3.1 g, 4.05 mmol) in $CHCl_3$–MeOH (1 : 1, 30 mL) was added $NaIO_4$ (1.127 g mg, 5.27 mmol) in water. The mixture was stirred 8 h at RT. Then the precipitate was filtered off and the solvent was evaporated. Chloroform was added and the insoluble inorganics were filtered again. The solvent was evaporated and the mixture dissolved in the mixture of chloroform-ether (4 : 1, v/v) and

hexane was added. The cloudy solution was left in fridge overnight. Then the mixture was filtered and the solvent removed under reduced pressure to obtain dialdehyde intermediate (2.6 g, 3.4 mmol) in 81% yield. HRMS-ESI: for $C_{41}H_{62}O_{13}$ 762.41904 Da, found *m*/*z* 785.40792 $[M + Na]^+$.

To a solution of dialdehyde (1.15 g, 1.51 mmol) and amine (290 mg, 1.51 mmol) in dry MeOH (11 mL) were added activated molecular sieves (4 Å; 250 mg), HOAc (181 mg, 3.02 mmol) and $NaCNBH_3$ (285 mg, 4.53 mmol). The reaction was stirred at RT for 1 h. The mixture was diluted with chloroform (100 mL) and washed with brine (2 × 100 mL) and dried over sodium sulphate. The solvent was evaporated under reduced pressure and the residue was chromatographed (i) $CHCl_3$–MeOH 100 : 1 v/v; (ii) AcOEt) to obtain product (510 mg, 0.55 mmol) as a colorless gel in 36% yield. This material was then lyophilized from 1,4-dioxane (white foam). $R_F = 0.4$ in DCM-MeOH 20 : 1 (v/v). ^{1}H NMR (400 MHz, $CDCl_3$) δ: 6.94 (d, $J = 2.1$ Hz, 1H), 6.74 (d, $J = 2.2$ Hz, 1H), 5.83 (t, $J = 1.7$ Hz, 1H), 4.97 (dd, $J = 18.3$, 1.8 Hz, 1H), 4.90–4.82 (m, 3H), 4.78 (dd, $J = 18.1$, 1.8 Hz, 1H), 4.34–4.25 (m, 2H), 4.21 (q, $J = 3.3$ Hz, 1H), 4.15 (q, $J = 3.2$ Hz, 1H), 4.00 (s, 1H), 3.87–3.73 (m, 3H), 3.72 (s, 2H), 3.21 (dd, $J = 9.3$, 3.0 Hz, 1H), 3.16 (dd, $J = 9.4$, 3.0 Hz, 1H), 3.03 (s, 1H), 2.95 (s, 1H), 2.90–2.65 (m, 4H), 2.36 (dd, $J = 13.0$, 9.5 Hz, 1H), 2.22 (s, 3H), 2.20–2.00 (m, 5H), 1.94–1.31 (m, 22H), 1.26–1.22 (m, 2H), 1.20 (d, $J = 4.7$ Hz, 3H), 1.18 (d, $J = 4.5$ Hz, 3H), 1.13 (d, $J = 6.3$ Hz, 3H), 0.89 (s, 3H), 0.83 (s, 3H); Fig. S5A. ^{13}C NMR (101 MHz, $CDCl_3$) δ: 174.83, 174.59, 153.88, 130.27, 129.70, 128.38, 121.93, 121.31, 117.53, 103.43, 98.18, 95.32, 85.51, 82.54, 81.73, 73.47, 73.00, 72.53, 68.30, 68.02, 66.43, 66.35, 64.57, 62.13, 50.57, 49.68, 49.61, 41.75, 40.01, 37.12, 36.67, 36.21, 35.68, 35.38, 35.13, 33.08, 30.17, 29.75, 26.86, 26.62, 26.53, 23.59, 21.37, 21.13, 20.39, 19.74, 18.16, 15.77; Fig. S5B. HRMS-ESI: for $C_{50}H_{74}N_4O_{12}$ calcd 922.53032 Da, found *m*/*z* 923.53887 $[M + H]^+$, 945.51898 $[M + Na]^+$, 462.27280 $[M + H]^{2+}$, 473.26389 $[M + Na]^{2+}$, 481.25027 $[M + K]^{2+}$; Fig. S5C. HPLC: $R_T = 2.953$ min; purity 98%; Fig. S5D.

5.1.8 General procedure for CuAAC. To the mixture of **DgA** (1 equiv.), corresponding fluorophore (1 equiv.) and TBTA (5 mol%) in dry DMF (5 mL) sodium ascorbate (30 μL of 1 M solution) and $CuSO_4 \cdot 5H_2O$ (30 μL of 1 M solution) were added. The mixture was stirred 12 h at RT. The solvents were evaporated and the residue was purified by column chromatography. The product thus obtained was lyophilized from 1,4-dioxane.

*5.1.8.1 Digitoxin-BODIPY (**FD1**).* In reaction: **DgA** (92 mg, 0.1 mmol), BODIPY **F1** (25 mg, 0.1 mmol). Chromatography: AcOEt-MeOH 100 : 1 to 10 : 1 (v/v). The product (67 mg, 0.057 mmol) was obtained as slightly yellowish lyophilizate in 57% yield. $R_F = 0.35$ in AcOEt. ^{1}H NMR (400 MHz, $CDCl_3$) δ: 7.75 (s, 1H), 7.66 (t, $J = 5.0$ Hz, 1H), 7.49 (s, 1H), 7.08 (s, 2H), 7.01 (d, $J = 2.1$ Hz, 1H), 6.79 (d, $J = 2.1$ Hz, 1H), 6.41 (s, 2H), 5.84 (t, $J = 1.7$ Hz, 1H), 5.51 (s, 2H), 4.97 (dd, $J = 18.3$, 1.8 Hz, 1H), 4.91–4.82 (m, 5H), 4.78 (dd, $J = 18.2$, 1.8 Hz, 1H), 4.23 (q, $J = 3.3$ Hz, 1H), 4.19 (q, $J = 3.2$ Hz, 1H), 4.02 (s, 1H), 3.89–3.75 (m, 3H), 3.75–3.71 (m, 2H), 3.23 (dd, $J = 9.3$, 3.0 Hz, 1H), 3.18 (dd, $J = 9.4$, 2.9 Hz, 1H), 3.02 (s, 1H), 2.93 (s, 1H), 2.86 (dd, $J = 13.0$, 2.3 Hz, 1H), 2.81–2.72 (m, 3H), 2.43 (dd, $J = 13.0$, 9.2 Hz, 1H), 2.21 (s, 3H), 2.19–2.02 (m, H), 1.98–1.79 (m, 4H), 1.79–1.30 (m, 20H), 1.22 (d, $J = 6.4$ Hz, 3H), 1.20 (d, $J = 6.4$ Hz, 3H), 1.15 (d, $J = 6.3$ Hz, 3H), 0.91 (s, 3H), 0.85 (s, 3H); Fig. S6A. ^{13}C NMR (101 MHz, $CDCl_3$) δ: 174.93, 174.76, 153.85, 147.87, 141.10, 130.58, 130.48, 129.03, 122.60, 121.78, 121.01, 117.70, 103.38, 98.31, 95.46, 85.72, 82.69, 81.89, 73.61, 72.68, 72.47, 72.45, 68.39, 68.16, 66.57, 64.39, 61.90, 51.04, 50.24, 49.73, 49.66, 42.90, 41.92, 40.15, 37.27, 36.84, 36.34, 35.83, 35.44, 35.28, 33.26, 30.30, 29.88, 26.99, 26.77, 26.66, 23.73, 21.51, 21.26, 20.48, 20.12, 18.31, 18.29, 15.89; Fig. S6B. HRMS-ESI: for $C_{62}H_{84}BF_2N_7O_{12}$ + Na calcd 1190.61313 Da, found *m*/*z* 1190.61452; for $C_{62}H_{84}BF_2N_7O_{12}$ + K calcd 1206.58707, found *m*/*z* 1206.58815; Fig. S6C. HPLC: $R_T = 2.025$ min; purity ≥95%; Fig. S6D.

*5.1.8.2 Digitoxin-BODIPY (**FD2**).* In reaction: **DgA** (82 mg, 0.089 mmol), BODIPY **F2** (28 mg, 0.089 mmol). Chromatography: $CHCl_3$–MeOH 100 : 1 → 50 : 1 (v/v). The product (71 mg, 0.057) was obtained as orange lyophylizate in 64% yield. $R_F = 0.55$ in DCM-MeOH 20 : 1 (v/v). ^{1}H NMR (400 MHz, $CDCl_3$) δ: 7.40 (s, 1H), 6.96 (s, 1H), 6.76 (s, 1H), 5.97 (s, 2H), 5.83 (t, $J = 1.9$ Hz, 1H), 5.46 (s, 2H), 4.97 (dd, $J = 18.3$, 1.8 Hz, 1H), 4.86 (ddd, $J = 14.0$, 9.5, 2.0 Hz, 3H), 4.78 (dd, $J = 18.1$, 1.8 Hz, 1H), 4.22 (q, $J = 3.3$ Hz, 1H), 4.17 (q, $J = 3.2$ Hz, 1H), 4.01 (s, 1H), 3.85–3.69 (m, 5H), 3.22 (dd, $J = 9.3$, 3.0 Hz, 1H), 3.17 (dd, $J = 9.4$, 2.9 Hz, 1H), 3.01 (s, 1H), 2.98–2.91 (m, 2H), 2.86 (t, $J = 7.2$ Hz, 2H), 2.78–2.72 (m, 2H), 2.47 (s, 6H), 2.19 (s, 3H), 2.18 (s, 6H), 2.15–2.03 (m, 5H), 1.95–1.32 (m, 26H), 1.21 (d, $J = 6.2$ Hz, 3H), 1.18 (d, $J = 6.2$ Hz, 3H), 1.13 (d, $J = 6.3$ Hz, 3H), 0.89 (s, 3H), 0.84 (s, 3H); Fig. S7A. ^{13}C NMR (101 MHz, $CDCl_3$) δ: 174.89, 174.65, 153.95, 153.58, 146.78, 145.89, 140.48, 131.45, 130.22, 128.85, 121.68, 121.55, 121.30, 117.64, 103.36, 98.26, 95.41, 85.60, 82.66, 81.88, 73.54, 72.64, 68.33, 68.11, 66.53, 64.44, 61.97, 51.02, 50.23, 49.70, 48.86, 41.84, 40.10, 37.22, 36.80, 36.31, 35.78, 35.49, 35.24, 33.19, 31.70, 30.27, 27.76, 26.93, 26.73, 26.63, 26.08, 23.69, 21.47, 21.22, 20.45, 20.02, 18.26, 18.25, 16.21, 15.85, 14.51 (t, $J_{C,F} = 2.5$ Hz); Fig. S7B. HRMS-ESI: for $C_{68}H_{95}BF_2N_6O_{12}$ + H calcd 1237.71419 Da, found *m*/*z* 1237.71724; for $C_{68}H_{95}BF_2N_6O_{12}$ + Na calcd 1259.69613, found *m*/*z* 1259.69832; Fig. S7C. HPLC: $R_T = 2.947$ min; purity 96%; Fig. S7D.

*5.1.8.3 Digitoxin-BODIPY (**FD3**).* In reaction: **DgA** (76 mg, 0.082 mmol), BODIPY **F3** (34 mg, 0.082 mmol). Chromatography: $CHCl_3$–MeOH 100 : 1 → 50 : 1 (v/v). The product (62 mg, 0.046 mmol) was obtained as a pink lyophilizate in 56% yield. $R_F = 0.4$ in DCM-MeOH 20 : 1 (v/v). ^{1}H NMR (400 MHz, $CDCl_3$) δ: 7.52 (d, $J = 16.3$ Hz, 1H), 7.45 (s, 1H), 7.15 (t, $J = 7.8$ Hz, 1H), 7.11–6.97 (m, 3H), 6.80 (dd, $J = 8.0$, 1.6 Hz, 1H), 6.77 (s, 1H), 6.54 (s, 1H), 6.00 (s, 1H), 5.83 (t, $J = 1.7$ Hz, 1H), 5.47 (s, 2H), 4.96 (dd, $J = 18.4$, 1.8 Hz, 1H), 4.90–4.81 (m, 3H), 4.76 (dd, $J = 18.3$, 1.7 Hz, 1H), 4.24 (q, $J = 3.3$ Hz, 1H), 4.17 (q, $J = 3.2$ Hz, 1H), 4.00 (s, 1H), 3.84–3.68 (m, 5H), 3.22 (dd, $J = 9.2$, 2.9 Hz, 1H), 3.15 (dd, $J = 9.4$, 2.9 Hz, 1H), 2.93 (q, $J = 7.4$ Hz, 2H), 2.86 (t, $J = 7.2$ Hz, 2H), 2.74 (dd, $J = 8.7$, 5.5 Hz, 2H), 2.49 (s, 3H), 2.19 (s, 6H), 2.15–2.06 (m, 5H), 1.96–1.29 (m, 26H), 1.21 (d, $J = 6.2$ Hz, 3H), 1.17 (d, $J = 6.2$ Hz, 3H), 1.11 (d, $J = 6.3$ Hz, 3H), 0.88 (s, 3H), 0.83 (s, 3H); Fig. S8A. ^{13}C NMR (101 MHz, $CDCl_3$) δ: 174.94, 174.72, 156.75, 154.00, 151.15, 146.65, 144.49, 140.45, 139.92, 137.94, 135.47, 132.65, 131.87, 130.32, 129.80, 121.87, 121.44, 121.44, 119.63, 119.10, 118.06, 117.52, 116.30, 113.81, 98.21, 95.35, 85.52, 82.48, 81.73, 73.50, 72.67, 68.25, 68.11, 66.55, 66.43, 50.94,

49.59, 48.91, 41.71, 39.99, 37.07, 36.69, 36.19, 35.66, 35.12, 33.08, 31.64, 30.18, 29.68, 27.67, 26.84, 26.61, 26.49, 25.87, 23.59, 21.35, 21.13, 20.36, 19.91, 18.15, 16.31, 16.16, 15.75, 14.59 (t, $J_{C,F}$ = 2.0 Hz); Fig. S8B. HRMS-ESI: for $C_{75}H_{99}BF_2N_6O_{13}$ + H 1341.74040 Da, found *m*/*z* 1341.74375; for $C_{75}H_{99}BF_2N_6O_{13}$ + Na calcd 1363.72234 found *m*/*z* 1363.72503; Fig. S8C. HPLC: R_T = 3.911 min; purity 97%; Fig. S8D.

*5.1.8.4 Digitoxin-BODIPY (**FD4**).* In reaction: **DgA** (74 mg, 0.08 mmol), BODIPY **F4** (36 mg, 0.08 mmol). Chromatography: $CHCl_3$–MeOH 100 : 1 → 40 : 1 (v/v). The product (68 mg, 0.05 mmol) was obtained as a blue lyophilizate in 63% yield. R_F = 0.45 in DCM-MeOH 20 : 1 (v/v). ^{1}H NMR (400 MHz, $CDCl_3$) δ: 7.49–7.43 (m, 2H), 7.41 (d, J = 16.3 Hz, 1H), 7.16 (d, J = 16.2 Hz, 1H), 6.97 (s, 1H), 6.77 (s, 1H), 6.69–6.61 (m, 2H), 6.59 (s, 1H), 5.97 (s, 1H), 5.84 (t, J = 1.8 Hz, 1H), 5.47 (s, 2H), 4.97 (dd, J = 18.3, 1.8 Hz, 1H), 4.86 (td, J = 9.8, 2.0 Hz, 3H), 4.78 (dd, J = 18.1, 1.8 Hz, 1H), 4.22 (q, J = 3.3 Hz, 1H), 4.17 (q, J = 3.2 Hz, 1H), 4.01 (s, 1H), 3.85–3.70 (m, 5H), 3.22 (dd, J = 9.3, 3.1 Hz, 1H), 3.16 (dd, J = 9.4, 3.0 Hz, 1H), 3.00 (s, 6H), 2.87 (t, J = 7.3 Hz, 4H), 2.76 (dd, J = 8.8, 5.6 Hz, 2H), 2.51 (s, 3H), 2.23 (s, 3H), 2.20 (s, 6H), 2.17–2.05 (m, 5H), 1.98–1.28 (m, 26H), 1.21 (d, J = 6.2 Hz, 3H), 1.18 (d, J = 6.2 Hz, 3H), 1.13 (d, J = 6.3 Hz, 3H), 0.90 (s, 3H), 0.84 (s, 3H); Fig. S9A. ^{13}C NMR (101 MHz, $CDCl_3$) δ: 174.83, 174.66, 153.62, 151.69, 151.08, 146.96, 142.80, 140.59, 138.26, 137.39, 133.06, 131.24, 130.26, 129.22, 124.71, 121.63, 121.00, 118.24, 117.70, 114.36, 112.10, 98.27, 95.44, 85.67, 82.67, 81.88, 73.55, 72.66, 68.36, 68.14, 66.55, 51.04, 49.70, 48.91, 41.89, 40.34, 40.14, 37.25, 36.82, 36.33, 35.81, 35.26, 33.23, 31.85, 30.29, 29.86, 27.71, 26.96, 26.75, 26.65, 26.09, 23.71, 21.49, 21.24, 20.49, 20.05, 18.28, 16.58, 16.16, 15.87, 14.58 (t, $J_{C,F}$ = 2.3 Hz); Fig. S9B. HRMS-ESI: for $C_{77}H_{104}BF_2N_7O_{12}$ + H calcd 1368.78768 Da, found *m*/*z* 1368.78931; 1390.77087 $[M + Na]^+$; for $C_{77}H_{104}BF_2N_7O_{12}$ + Na calcd 1390.76963 Da found *m*/*z* 1390.77087; Fig. S9C. HPLC: R_T = 2.688 min; purity 98%; Fig. S9D.

*5.1.8.5 Digitoxin-coumarin (**FD5**).* In reaction: **DgA** (92 mg, 0.1 mmol), coumarin **F5** (25 mg, 0.1 mmol). Chromatography: DCM-MeOH 40 : 1 (v/v); AcOEt to AcOEt-MeOH 10 : 1 (*v*/*v*). The product (79 mg, 0.065 mmol) was obtained as slightly yellowish lyophilizate in 65% yield. R_F = 0.4 in DCM-MeOH 20 : 1 (v/v). ^{1}H NMR (400 MHz, $CDCl_3$) δ: 9.16 (t, J = 5.8 Hz, 1H), 8.66 (s, 1H), 7.64 (s, 1H), 7.40 (d, J = 9.0 Hz, 1H), 6.93 (d, J = 2.1 Hz, 1H), 6.73 (d, J = 2.1 Hz, 1H), 6.63 (dd, J = 9.0, 2.5 Hz, 1H), 6.47 (d, J = 2.4 Hz, 1H), 5.85 (t, J = 1.8 Hz, 1H), 5.49–5.45 (m, 2H), 4.99 (dd, J = 18.2, 1.8 Hz, 1H), 4.91–4.86 (m, 2H), 4.84 (dd, J = 9.7, 2.0 Hz, 1H), 4.79 (dd, J = 18.1, 1.8 Hz, 1H), 4.70 (s, 1H), 4.68 (s, 1H), 4.22 (q, J = 3.4 Hz, 1H), 4.18 (q, J = 3.2 Hz, 1H), 4.01 (s, 1H), 3.89–3.65 (m, 5H), 3.44 (q, J = 7.1 Hz, 4H), 3.21 (ddd, J = 12.2, 9.3, 3.0 Hz, 2H), 3.02 (s, 1H), 2.97 (s, 1H), 2.90–2.82 (m, 1H), 2.81–2.68 (m, 3H), 2.38 (dd, J = 13.0, 9.4 Hz, 1H), 2.18 (s, 3H), 2.16–2.01 (m, 5H), 1.96–1.32 (m, 22H), 1.24 (s, 3H), 1.22 (s, 3H), 1.22 (s, 3H), 1.20 (s, 3H), 1.15 (d, J = 6.3 Hz, 3H), 0.90 (s, 3H), 0.85 (s, 3H); Fig. S10A. ^{13}C NMR (101 MHz, $CDCl_3$) δ: 174.77, 174.64, 163.33, 162.63, 157.79, 153.66, 152.74, 148.22, 145.11, 131.24, 130.25, 130.08, 129.18, 128.75, 128.10, 122.61, 121.55, 121.50, 117.74, 110.08, 108.38, 103.41, 98.30, 96.67, 95.45, 85.69, 82.67, 81.81, 73.56, 72.89, 72.65, 68.45, 68.15, 66.55, 66.49, 64.64, 62.15, 51.05, 50.47, 49.72, 49.03, 45.20, 41.91, 40.16, 37.25, 36.82, 36.33, 35.82, 35.52, 35.45, 35.26, 33.25, 30.29, 29.87, 26.98, 26.76, 26.65, 23.71, 21.51, 21.25, 20.47, 20.00, 18.33, 18.27, 15.89, 12.53; Fig. S10B. HRMS-ESI: for $C_{67}H_{92}N_6O_{15}$ + Na calcd 1243.65129 Da, found *m*/*z* 1243.65271; for $C_{67}H_{92}N_6O_{15}$ + K calcd 1259.62522, found *m*/*z* 1259.62563; Fig. S10C. HPLC: R_T = 2.627 min; purity ≥98%; Fig. S10D.

*5.1.8.6 Digitoxin-Nile red (**FD6**).* In reaction: **DgA** (92 mg, 0.1 mmol), Nile red **F6** (37 mg, 0.1 mmol). Chromatography: $CHCl_3$–MeOH 100 : 1 → 40 : 1 (v/v); AcOEt → AcOEt-MeOH 10 : 1 (v/v). The product (86 mg, 0.066 mmol) was obtained as a violet lyophilizate in 66%. R_F = 0.4 in DCM-MeOH 20 : 1 (v/v). ^{1}H NMR (400 MHz, $CDCl_3$) δ: 8.20 (d, J = 8.8 Hz, 1H), 8.15 (d, J = 2.6 Hz, 1H), 7.58 (d, J = 9.1 Hz, 1H), 7.19 (dd, J = 8.7, 2.6 Hz, 1H), 6.98 (d, J = 2.1 Hz, 1H), 6.76 (d, J = 2.2 Hz, 1H), 6.65 (dd, J = 9.1, 2.7 Hz, 1H), 6.45 (d, J = 2.7 Hz, 1H), 6.29 (s, 1H), 5.86 (t, J = 1.7 Hz, 1H), 5.52 (s, 2H), 5.37 (s, 2H), 4.98 (dd, J = 18.3, 1.8 Hz, 1H), 4.90–4.82 (m, 4H), 4.80 (dd, J = 18.1, 1.8 Hz, 1H), 4.22 (q, J = 3.4 Hz, 1H), 4.17 (q, J = 3.1 Hz, 1H), 4.01 (s, 1H), 3.88–3.67 (m, 5H), 3.46 (q, J = 7.1 Hz, 4H), 3.22 (dd, J = 9.3, 3.0 Hz, 1H), 3.17 (dd, J = 9.4, 3.0 Hz, 1H), 3.01 (s, 1H), 2.93 (s, 1H), 2.89–2.82 (m, 1H), 2.81–2.71 (m, 3H), 2.40 (dd, J = 13.0, 9.3 Hz, 1H), 2.19 (s, 3H), 2.17–2.02 (m, 5H), 1.95–1.31 (m, 26H), 1.26 (t, J = 7.1 Hz, 6H), 1.20 (t, J = 6.6 Hz, 6H), 1.15 (d, J = 6.3 Hz, 3H), 0.90 (s, 3H), 0.86 (s, 3H); Fig. S11A. ^{13}C NMR (101 MHz, $CDCl_3$) δ: 183.10, 174.61, 174.50, 160.88, 153.62, 152.11, 150.81, 146.88, 143.52, 139.71, 134.09, 131.16, 130.24, 130.12, 128.75, 127.83, 126.02, 124.71, 123.08, 121.49, 121.25, 118.21, 117.63, 109.59, 107.01, 105.26, 103.27, 98.18, 96.27, 95.33, 85.59, 82.56, 81.72, 73.42, 72.53, 68.27, 68.02, 66.44, 64.43, 62.56, 61.92, 50.93, 50.21, 49.58, 49.12, 45.08, 41.80, 40.05, 37.14, 36.69, 36.20, 35.70, 35.38, 35.14, 33.14, 30.17, 29.75, 26.86, 26.64, 26.53, 23.59, 21.39, 21.13, 20.34, 19.95, 18.18, 18.15, 15.76, 12.61; Fig. S11B. HRMS-ESI: for $C_{73}H_{94}N_6O_{15}$ + Na calcd 1317.66694 Da, found *m*/*z* 1317.66788 $[M + Na]^+$; for $C_{73}H_{94}N_6O_{15}$ + K calcd 1333.64087, 1333.64191; Fig. S11C. HPLC: R_T = 2.662 min; purity 95%; Fig. S11D.

*5.1.8.7 Digitoxin-fluorescein (**FD7**).* In reaction: **DgA** (92 mg, 0.1 mmol), fluorescein **F7** (45 mg, 0.1 mmol). Chromatography: $CHCl_3$–MeOH 100 : 1 → 40 : 1 (v/v), AcOEt to AcOEt-MeOH 10 : 1 (v/v). The product (93 mg, 0.07 mmol) was obtained as an orange lyophilizate in 70%. R_F = 0.4 in DCM-MeOH 20 : 1 (v/v). ^{1}H NMR (400 MHz, $CDCl_3$) δ: 8.23 (dd, J = 7.7, 1.5 Hz, 1H), 7.77 (s, 1H), 7.71 (td, J = 7.5, 1.5 Hz, 1H), 7.65 (td, J = 7.6, 1.4 Hz, 1H), 7.28 (dd, J = 7.5, 1.4 Hz, 1H), 7.23 (dd, J = 7.3, 2.2 Hz, 1H), 7.06 (d, J = 2.4 Hz, 1H), 6.97 (d, J = 2.1 Hz, 1H), 6.88 (d, J = 8.9 Hz, 1H), 6.85 (d, J = 9.7 Hz, 1H), 6.79 (dd, J = 9.0, 2.4 Hz, 1H), 6.77 (d, J = 2.1 Hz, 1H), 6.52 (dd, J = 9.7, 1.9 Hz, 1H), 6.44 (d, J = 1.9 Hz, 1H), 5.84 (t, J = 1.8 Hz, 1H), 5.51 (s, 2H), 5.48 (s, 1H), 5.23 (s, 2H), 4.99 (dd, J = 18.3, 1.8 Hz, 1H), 4.90–4.83 (m, 3H), 4.79 (dd, J = 18.1, 1.8 Hz, 1H), 4.22 (q, J = 3.3 Hz, 1H), 4.18 (q, J = 3.2 Hz, 1H), 4.01 (qt, J = 7.1, 3.4 Hz, 2H), 3.87–3.65 (m, 5H), 3.22 (dd, J = 9.3, 3.0 Hz, 1H), 3.18 (dd, J = 9.4, 2.9 Hz, 1H), 3.03 (s, 1H), 2.85 (dd, J = 12.5, 2.4 Hz, 1H), 2.76 (t, J = 7.1 Hz, 3H), 2.42 (dd, J = 13.0, 9.3 Hz, 1H), 2.19 (s, 3H), 2.16–2.01 (m, 5H), 1.97–1.33 (m, 22H), 1.21 (d, J = 4.3 Hz, 3H), 1.19 (d, J = 4.1 3H), 1.15 (d, J = 6.3 Hz, 3H), 0.94 (t, J = 7.1 Hz, 3H), 0.90 (s, 3H), 0.85 (s,

3H); Fig. S12A. ^{13}C NMR (101 MHz, $CDCl_3$) δ: 185.83, 174.85, 174.66, 165.41, 162.71, 158.98, 154.13, 153.74, 150.29, 142.54, 134.25, 132.67, 131.32, 130.79, 130.49, 130.43, 130.38, 130.33, 130.05, 129.78, 129.17, 128.91, 128.76, 128.08, 123.62, 121.66, 121.19, 117.93, 117.69, 115.39, 113.60, 105.90, 103.37, 101.54, 98.31, 95.44, 85.63, 82.69, 81.90, 73.56, 72.66, 68.36, 68.13, 66.57, 66.53, 64.44, 64.25, 62.62, 61.98, 61.46, 54.20, 51.05, 50.30, 49.72, 49.25, 41.88, 40.15, 37.26, 36.83, 36.33, 35.80, 35.49, 35.26, 33.22, 30.29, 29.86, 26.97, 26.74, 26.65, 23.71, 21.50, 21.24, 20.45, 20.09, 18.30, 18.26, 15.89, 13.70; Fig. S12B. HRMS-ESI: for $C_{75}H_{92}N_4O_{17}$ + H calcd 1321.65302 Da, found *m*/*z* 1321.65522; for $C_{75}H_{92}N_4O_{17}$ + Na calcd 1343.63497, found *m*/*z* 1343.63625; for $C_{75}H_{92}N_4O_{17}$ + K calcd 1359.60891, found *m*/*z* 1359.60996; Fig. S12C. HPLC: R_T = 2.946 min; purity 97%; Fig. S12D.

*5.1.8.8 Digitoxin-rhodamine (**FD8**).* In reaction: **DgA** (87 mg, 0.094 mmol), rhodamine **F8** (50 mg, 0.094 mmol). Chromatography: $CHCl_3$–MeOH 20 : 1 (v/v) followed by purification using preparative TLC ($CHCl_3$–MeOH 60 : 1, (v/v). The product (77 mg, 0.054 mmol) was obtained as red colored lyophilizate in 57% yield. R_F = 0.5 in DCM-MeOH 10 : 1 (v/v). ^{1}H NMR (400 MHz, CD_3OD) δ: 7.97–7.85 (m, 1H), 7.77–7.70 (m, 2H), 7.70–7.66 (m, 1H), 7.51–7.43 (m, 1H), 7.36 (s, 1H), 7.35–7.25 (m, 2H), 7.20 (d, J = 4.3 Hz, 1H), 7.18 (d, J = 4.3 Hz, 1H), 7.05 (dd, J = 9.6, 2.5 Hz, 1H), 7.00 (d, J = 2.5 Hz, 1H), 6.98 (s, 2H), 6.96–6.94 (m, 1H), 6.89–6.79 (m, 2H), 5.89 (t, J = 1.7 Hz, 1H), 5.54 (s, 1H), 5.39 (s, 1H), 5.02 (dd, J = 18.6, 1.8 Hz, 1H), 4.94–4.87 (m, 5H), 4.34 (s, 2H), 4.24 (q, J = 3.0 Hz, 1H), 4.21 (q, J = 3.1 Hz, 1H), 4.01 (s, 1H), 3.90–3.77 (m, 5H), 3.75–3.66 (m, 8H), 3.23 (d, J = 3.0 Hz, 1H), 3.20 (d, J = 2.9 Hz, 1H), 2.85–2.79 (m, 2H), 2.79–2.67 (m, 3H), 2.63 (s, 1H), 2.44 (dd, J = 13.1, 8.9 Hz, 1H), 2.23–2.18 (m, 2H), 2.17 (s, 3H), 2.06–1.36 (m, 27H), 1.33 (t, J = 7.2 Hz, 12H), 1.20 (d, J = 6.2 Hz, 3H), 1.18 (d, J = 6.3 Hz, 3H), 1.09 (d, J = 6.2 Hz, 2H), 0.93 (s, 3H), 0.87 (s, 3H); Fig. 1A. ^{13}C NMR (101 MHz, CD_3OD) δ: 177.06, 175.80, 168.82, 157.69, 155.75, 155.40, 153.35, 142.12, 135.58, 135.43, 131.70, 130.71, 130.22, 129.85, 129.61, 129.27, 128.61, 128.32, 128.13, 127.67, 127.18, 123.51, 122.19, 121.15, 116.37, 113.78, 113.36, 103.93, 99.09, 95.88, 95.48, 85.02, 82.33, 81.41, 73.93, 73.07, 72.14, 68.19, 68.04, 67.04, 66.71, 63.53, 60.86, 53.49, 50.69, 49.65, 48.78, 45.50, 41.45, 41.27, 39.53, 37.53, 37.12, 37.06, 36.56, 35.43, 35.03, 34.92, 31.99, 29.98, 29.59, 26.66, 26.47, 26.10, 22.90, 21.17, 20.95, 19.10, 18.94, 17.21, 17.08, 15.01, 11.56; Fig. S13B. HRMS-ESI: for $C_{82}H_{110}N_7O_{14}^+$ calcd 1416.81053 Da, found *m*/*z* 1416.81186; for $C_{82}H_{110}N_7O_{14}$ + H $[M + H]^{2+}$ calcd 708.90890 found 708.90852; for $C_{82}H_{110}N_7O_{14}$ + Na $[M + Na]^{2+}$ calcd 719.89987 Da, found *m*/*z* 719.89934; Fig. S13C. HPLC: R_T = 2.931 min; purity 96%; Fig. S13D.

*5.1.8.9 Digitoxin-FITC (**FD9**).* In reaction: **DgA** (92 mg, 0.1 mmol), FITC **F9** (62 mg, 0.1 mmol). Chromatography: DCM-MeOH 25 : 1 → 10 : 1 (v/v). The product (96 mg, 0.062 mmol) was obtained as slightly orange lyophilizate in 62% yield. R_F = 0.3 in DCM-MeOH 20 : 1 (v/v). ^{1}H NMR (400 MHz, CD_3OD) δ: 8.22 (d, J = 2.0 Hz, 1H), 7.85–7.75 (m, 2H), 7.09 (d, J = 8.2 Hz, 1H), 6.94 (d, J = 2.1 Hz, 1H), 6.78 (d, J = 2.2 Hz, 1H), 6.67 (d, J = 2.3 Hz, 3H; overlap), 6.65 (d, J = 2.1 Hz, 1H), 6.51 (qd, J = 7.9, 2.3 Hz, 2H), 5.87 (t, J = 1.6 Hz, 1H), 5.43 (s, 2H), 5.03 (dd, J = 18.5, 1.8 Hz, 1H), 4.93–4.84 (m, 6H), 4.54 (s, 2H), 4.24 (q, J = 3.2 Hz, 1H), 4.20 (q, J = 3.0 Hz, 1H), 4.00 (t, J = 2.9 Hz, 1H), 3.80 (tdd, J = 15.1, 12.3, 7.8 Hz, 6H), 3.72–3.65 (m, 4H), 3.63 (s, 4H), 3.61 (s, 4H), 3.59 (s, 4H), 3.22 (dd, J = 4.2, 2.8 Hz, 1H), 3.20 (dd, J = 4.2, 2.9 Hz, 1H), 2.84–2.78 (m, 2H), 2.75–2.67 (m, 2H), 2.41 (dd, J = 13.0, 9.1 Hz, 1H), 2.16 (s, 3H), 2.06–1.31 (m, 25H), 1.25 (s, 1H), 1.22 (s, 1H), 1.20 (d, J = 3.7 Hz, 3H), 1.19 (d, J = 3.7 Hz, 3H), 1.09 (d, J = 6.2 Hz, 3H), 0.92 (s, 3H), 0.86 (s, 3H); Fig. S14A. ^{13}C NMR (101 MHz, CD_3OD) δ: 177.47, 176.40, 170.30, 154.03, 153.37, 144.78, 130.62, 130.34, 129.59, 128.98, 124.85, 124.30, 122.46, 121.57, 117.04, 113.02, 110.75, 104.41, 102.87, 99.55, 95.96, 85.56, 82.91, 81.99, 78.62, 78.30, 77.97, 75.23, 74.47, 73.55, 72.87, 70.66, 70.60, 70.54, 70.49, 69.90, 69.20, 68.74, 68.60, 67.47, 67.18, 64.51, 64.24, 61.70, 58.30, 51.30, 50.42, 50.23, 49.42, 44.67, 41.78, 40.18, 37.98, 37.58, 37.00, 36.00, 35.48, 32.64, 30.53, 30.14, 27.24, 27.01, 26.71, 23.59, 21.73, 21.51, 19.90, 19.60, 17.94, 17.81, 15.73; Fig. S14B. HRMS-ESI: for $C_{82}H_{106}N_6O_{21}S$ + Na calcd 1565.70241 Da, found *m*/*z* 1565.70481; for $C_{82}H_{106}N_6O_{21}S$ + 2Na 794.34565 $[M + 2Na]^{2+}$ calcd 794.34581, found *m*/*z* 794.34585; Fig. S14C. HPLC: R_T = 2.936 min; purity 98%; Fig. S14D.

*5.1.8.10 Digitoxin-TAMRA (**FD10**).* In reaction: **DgA** (36 mg, 0.039 mmol), TAMRA **F10** (25 mg, 0.039 mmol). Chromatography: DCM-MeOH 20 : 1 → 3 : 2 (*v*/*v*). The product (33 mg, 0.021 mmol) was obtained as a slightly orange lyophilizate in 54% yield. R_F = 0.3 in DCM-MeOH 5 : 1 (v/v). ^{1}H NMR (400 MHz, $CDCl_3$) δ: 8.39 (s, 0.6H, isomer), 8.18 (dd, J = 8.0, 1.6 Hz, 0.6H, isomer), 8.08–7.98 (m, 1H), 7.65–7.56 (m, 1H), 7.48 (s, 0.6H, isomer), 7.21 (d, J = 8.1 Hz, 0.6H, isomer), 6.92 (t, J = 2.6 Hz, 1H), 6.73 (t, J = 2.9 Hz, 1H), 6.63–6.52 (m, 2H), 6.47 (d, J = 2.6 Hz, 2H), 6.46 (d, J = 2.7 Hz, 0.6H, isomer), 6.35 (dq, J = 12.8, 9.9 Hz, 2H), 5.85 (t, J = 1.8 Hz, 1H), 5.43 (s, 1H), 5.40 (d, J = 3.2 Hz, 0.6H, isomer), 4.98 (dd, J = 18.2, 1.8 Hz, 1H), 4.90–4.82 (m, 3H), 4.79 (dd, J = 18.2, 1.7 Hz, 1H), 4.59 (s, 1H), 4.51 (s, 0.6H, isomer), 4.22 (q, J = 3.3 Hz, 1H), 4.17 (q, J = 3.1 Hz, 1H), 4.01 (s, 1H), 3.86–3.70 (m, 5H), 3.69 (s, 3H), 3.66 (s, 3H), 3.65–3.43 (m, 12H), 3.22 (dd, J = 9.2, 3.0 Hz, 1H), 3.19 (dd, J = 9.3, 3.0 Hz, 1H), 2.99–2.94 (m, 12H), 2.85–2.70 (m, 4H), 2.43–2.32 (m, 1H), 2.17–2.02 (m, 6H), 1.96–1.34 (m, 22H), 1.20 (t, J = 5.9 Hz, 6H), 1.12 (dd, J = 6.3, 4.3 Hz, 2H), 0.90 (s, 3H), 0.85 (s, 3H); Fig. S15A. ^{13}C NMR (101 MHz, $CDCl_3$) δ: 174.69, 174.53, 166.11, 166.06, 153.58, 153.02, 152.27, 136.28, 130.17, 128.94, 128.76, 128.60, 125.50, 124.60, 123.36, 122.99, 122.27, 121.53, 121.47, 121.32, 117.60, 108.96, 108.82, 106.39, 103.21, 98.41, 98.18, 95.33, 85.55, 82.55, 81.67, 73.44, 72.54, 70.46, 70.32, 70.27, 70.06, 69.75, 69.57, 69.51, 69.42, 68.30, 68.04, 66.43, 66.34, 64.53, 64.41, 61.90, 50.93, 50.26, 49.59, 48.87, 41.78, 40.26, 40.24, 40.09, 40.04, 37.14, 36.69, 36.21, 35.69, 35.34, 35.14, 34.21, 33.12, 30.30, 30.18, 29.75, 26.85, 26.63, 26.53, 23.60, 21.38, 21.13, 20.32, 19.86, 18.19, 18.16, 15.76; Fig. S15B. HRMS-ESI: for $C_{86}H_{115}N_7O_{20}$ + Na calcd 1588.80891 Da, found *m*/*z* 1588.81130; for $C_{86}H_{115}N_7O_{20}$ + Na 794.90849 $[M + Na]^{2+}$ calcd 794.90809 Da, found *m*/*z* 794.90849; for $C_{86}H_{115}N_7O_{20}$ + 2Na $[M + 2Na]^{2+}$ calcd 805.89907 Da, found *m*/*z* 805.89907; Fig. S15C. HPLC: R_T = 2.935 min; purity 99%; Fig. S15D.

5.2 *In silico* modeling

All the preparatory work for molecular docking, as well as molecular docking itself was done in Maestro 13.3 [graphical interface for Schrödinger Suite 2022-3 (Schrödinger, LLC, New York, NY, USA)]. Post-docking visualization was performed in PyMOL 2.5.0 (Schrödinger, LLC, New York, NY, USA). Ligands (Fig. 1) were converted to 3D structures, and their energy was minimized using LigPrep. NKA (7WYZ, conformation E2P, organism: *Squalus acanthias*)[52] in the E2P state with bound ouabain was obtained from the Protein Data Bank.[70] The NKA structure was stripped of all non-protein components except for ouabain to maintain proper conformation of the side chains during the energy minimization step and processed in the Protein Preparation Wizard, checking for the missing side chains and adding hydrogens corresponding to the pH of 7.4 using PROPKA. NKA with bound ouabain was minimized using OPLS4 force field and restrains RMSD cut-off 0.3 Å. Then, ouabain was removed from the minimized structure, and the cubic grid box ($55 \times 55 \times 55$ Å) with the center at 108.75, 97.66, and 120.13 was generated. This box also contained a sphere with the center at 108.01, 102.45, and 121.57, and a radius of 10 Å which served as a constraint for the lactone ring of CGs. Molecular docking itself was carried out using Glide 9.6 in flexible ligand mode with a rigid protein on extra precision.

Molecular dynamics simulations were done for ligands **FD10**, **FD9**, and **Dg** (reference structure) in a complex with NKA. Charges for the ligand atoms were computed using restrained electrostatic potential method based on wave function approximation using HF/6-31G*. The force field for the ligands was generated using General Amber Force Field and for NKA using AMBER99SB-ILDN with water type model TIP3P.[71] Complex of NKA with manually docked ligands was then converted into a box with periodic boundary condition, centered, solubilized and neutralized. Energy minimization, equilibration and molecular dynamics simulations were carried out using Gromacs 2021 and the standard protocol.[72] After the simulations (100 ns), periodic boundary condition was removed and all complexes where analyzed visually in PyMOL 3.1.2 with respect to the reference structure of **Dg**.

5.3 Cell lines and compounds

For this study, the following human cell lines were used: A549 (non-small cell lung adenocarcinoma, ATCC, USA), MRC-5 (noncancerous lung fibroblasts, Merck, USA), BJ (noncancerous foreskin fibroblasts, ATCC, USA), CCRF-CEM (acute lymphoblastic leukemia, ATCC, USA), K562 (chronic myelogenous leukemia, ATCC, USA), and U-2 OS (osteosarcoma, ATCC, USA), colorectal cancer cell lines HCT116 and HCT116p53−/− (lacking the p53 gene) were acquired from Horizon Discovery, the resistant clones CEM-DNR (resistant to daunorubicin) and K562-TAX (resistant to paclitaxel) were developed in the IMTM laboratory.[73]

All cell lines were cultured at 37 °C, 5% CO_2 in the atmosphere, and 95% humidity (standard conditions) and maintained at the exponential phase of growth. Briefly, every 2–3 days, the cells were washed with phosphate-buffered saline (PBS, pH 7,4) and detached from the surface of a cell culture dish (VWR, USA) by 0.25% trypsin with 0.02% ethylenediaminetetraacetic acid in Hanks' balanced solution (v/v) and transferred into a new cell culture dish. For cultivation of A549 and MRC-5 cells, high-glucose Dulbecco's modified Eagle's medium (DMEM) with 10% (v/v) fetal bovine serum (FBS; Merck, USA) and Eagle's minimum essential medium (MEM) with 10% FBS and 1% (v/v) nonessential amino acid solution were used, respectively, both with L-alanyl-L-glutamine (4 mM for DMEM and 2 mM for MEM). For cultivation of CCRF-CEM, CEM-DNR, and K562-TAX, RPMI 1640 medium supplemented with 10% FBS and 100 U mL^{-1} penicillin-streptomycin solution; K562, IMDM with 10% FBS and 100 U mL^{-1} penicillin-streptomycin solution; U-2 OS, HCT116, and HCT116p53−/−, McCoy's 5A medium with 10% FBS and 100 U mL^{-1} penicillin-streptomycin solution; BJ, EMEM with 10% FBS and 100 U mL^{-1} penicillin-streptomycin solution were used.

The tested compounds were prepared by conjugation of **Dg** with blue (**FD1**), green (**FD2**), yellow (**FD3**) and red (**FD4**) BODIPY, Nile red (**FD6**), coumarin (**FD5**), fluorescein (**FD7**), fluorescein isothiocyanate (**FD9**), 5(6)-carboxytetramethylrhodamine (**FD10**), and rhodamine (**FD8**). For the long-term storage, the tested compounds were diluted in anhydrous dimethyl sulfoxide (DMSO; purity: 99.7%, Merck, USA) at a concentration of 5 mM and stored in the dark at −20 °C in several aliquots.

5.4 Intracellular accumulation of Dg derivatives and partition coefficients

The A549 cells were seeded at the density of 0.75×10^5 cells per one mL into wells of 6-well plates and incubated at standard conditions for 24 h. Then, the cells were treated with **Dg** derivatives and the corresponding fluorophores at 0.5 μM concentration. After 3 h, the cells were washed with PBS, trypsinized, and resuspended in 0.5 mL of FluoroBrite™ DMEM. The suspension was then analyzed using flow cytometer BD FACSAria III; lasers and filters are specified in Table 6. The resulting cell counts corresponding to the fluorescence intensities were averaged over 10 000 events for each one of the three independent experiments using BD FACSDiva 8 software. For the comparison of accumulation rate of each derivative *vs.* the fluorophore, the ratios of their average fluorescence intensities was calculated. Moreover, the partition coefficients ($C\log P$, BioByte Corp.)[74] for each compound were calculated with ChemDraw Professional (17.0.0.206) using chemical properties module.

5.5 Cytotoxicity of Dg derivatives in cell monolayers

For cell viability assay, 5×10^3 and 1×10^4 of A549 and MRC-5 cells, respectively, were seeded into each well of flat-bottom 96-well plates (VWR, USA) in 100 μL of corresponding cell culture media and incubated for 24 h. Then, the cells were treated with the evaluated compounds diluted in 100 μL of cell culture media at 0.02–10 μM concentrations. As controls, cells treated only with cell culture medium and with medium including the vehicle (DMSO, at corresponding volume percentage) were

Table 6 Lasers and filters used in flow cytometry in order to evaluate intracellular accumulation of digitoxin (**Dg**) derivatives and the respective fluorophores contained in these compounds[a]

Compound	Laser [nm]	Filter [nm]
FD1/F1	405	525/50
FD2/F2	488	530/30
FD3/F3	488	575/26
FD4/F4	640	670/30
FD5/F5	405	525/50
FD6/F6	561	610/20
FD7/F7	488	530/30
FD8/F8	561	610/20
FD9/F9	488	530/30
FD10/F10	561	610/20

[a] **F1** – blue BODIPY, **F2** – green BODIPY, **F3** – yellow BODIPY, **F4** – red BODIPY, **F5** – coumarin, **F6** – Nile Red, **F7** – fluorescein, **F8** – rhodamine, **F9** – fluorescein isothiocyanate, **F10** – 5(6)-carboxytetramethylrhodamine.

used. After 72-h incubation, the medium was discarded, and the cells were washed with PBS and incubated for 2 h with 3 and 4 μL (for A549 and MRC-5, respectively) of WST-1 diluted in 100 μL of phenol red-free DMEM supplemented with 10% FBS. After 2 h, the absorbance was measured at 450 nm (reference at 650 nm) using a multi-plate reader (SUNRISE, Tecan, CHE). All measurements were performed in at least 3 independent measurements each consisting of 4 technical replicates. From the data the IC_{50}s and the standard errors of the means were calculated using GraphPad Prism 8.

For the MTS assay, cells were dispensed into 384-well microtiter plates at 30 μL per well. After 24 h, the test compounds were added using Echo550 acoustic liquid handler (Labcyte) to create dose–response curves with a 4-fold dilution. Each experiment included technical duplicates and was repeated in at least three independent biological replicates. Following a 72-h incubation in a humidified incubator, 4 μL of the MTS/PMS reagent was added to each well. After an additional 1–4 h of incubation, absorbance at 490 nm was measured on an EnVision Multilabel Plate Reader (PerkinElmer). IC_{50} values were determined from the resulting dose–response curves in Dotmatics software using the formula: $IC_{50} = (OD_{drugexposed\ cells}/\text{mean}\ OD_{control\ cells}) \times 100\%$.

5.6 Cytotoxicity of Dg derivatives in cancer cell spheroids

To determine the cytotoxicity of the evaluated compounds (Fig. 1) in a more complex cancer cell line model, cell spheroids were used because they better mimic the microenvironment in the tumor due to nutrient and oxygen gradient. The protocol for spheroid formation and drug treatment was adapted from ref. 75. First, the number of A549 cells for cell spheroid formation was optimized so that the spheroids have a diameter of 400 μm after 96 h of cultivation, the optimal number of cells was 3×10^3 per well. Briefly, A549 cells were seeded (3×10^3 per well in 100 μL) into wells of U-bottom 96-well plates with ultra-low attachment surface (Thermo Fisher Scientific, USA; VWR, USA). After 96 h of cultivation at standard conditions, the cancer cell spheroids were treated with a concentration series of **Dg** and its derivatives (0.2, 1, 5, 10, and 25 μM). Nontreated spheroids cultivated only in cell culture medium served as negative controls. After 72 h and, then, twice a week, the spheroids were regularly monitored using bright-field microscopy (inverted Olympus IX-83 microscope, dry 10× objective with the numerical aperture of 0.3, Olympus, Japan). After imaging, a total of 100 μL of the cultivation medium was carefully aspirated from each well and changed to a fresh cell culture medium.

The captured microscopic images of the cell spheroids were analyzed using AnaSP® 1.4 software[44] running on Matlab (R2022a). First, image segmentation was performed automatically by the AnaSP® (unrecognized images were, if possible, segmented manually), and then, data extraction from the segmented images was performed automatically by AnaSP® (in ref. 75) which yielded a list of values of morphological parameters (area, volume, equivalent diameter, sphericity, circularity, solidity, and compactness) for each spheroid at all time points. The means and the standard errors of the means were calculated (GraphPad Prism 8) from three independent experiments each consisting of three technical replicates.

5.7 Intracellular localization of Dg derivatives

The intracellular localization of **Dg** derivatives in living cells (A549 and MRC-5) was studied using live-cell fluorescence microscopy. For this experiment, A549 and MRC-5 cells were seeded into 4-chamber glass-bottom dishes (MatTek Corporation, USA) and incubated for 16 h at standard conditions. Then, the cells were treated with **Dg** derivatives at concentrations and times given in Table 7. The compounds were diluted in DMEM and MEM for A549 and MRC-5, respectively. After the incubation period, the cells were gently washed with PBS which was replaced with FluoroBrite™ DMEM (Gibco™, USA). During the microscopy, the cells were kept at 37 °C, 5% CO_2 in the atmosphere, and 95% humidity. The imaging was done by an inverse fluorescence

Table 7 Concentrations and incubation times of digitoxin (**Dg**) derivatives used to evaluate their intracellular localization by fluorescence microscopy[a]

Cell line	Parameter	FD1	FD2	FD3	FD4	FD5	FD6	FD7	FD8	FD9	FD10
A549	c [nM]	500	500	500	500	500	500	500	50	500	500
	t [h]	3	3	3	4	3	4	4	5	5	4
MRC-5	c [nM]	500	500	500	500	500	500	500	50	500	500
	t [h]	5	3	4.5	4.5	5	5	5	5	5	5

[a] **F1** – blue BODIPY, **F2** – green BODIPY, **F3** – yellow BODIPY, **F4** – red BODIPY, **F5** – coumarin, **F6** – Nile Red, **F7** – fluorescein, **F8** – rhodamine, **F9** – fluorescein isothiocyanate, **F10** – 5(6)-carboxytetramethylrhodamine.

Table 8 Lasers and filters used during flow cytometry for cell death evaluation

Kit	Laser [nm]	Filter [nm]
Alexa Fluor® 488 annexin V	488	530/30
Propidium iodide	488	575/26
CFBlue annexin V	405	450/50
7-Aminoactinomycin D	561	670/30

microscope Olympus IX-81 (Olympus, Japan) using a 60× oil immersion objective with the numerical aperture of 1.4 (Olympus, Japan) and EM-CCD camera (Hamamatsu, Japan). During imaging and post-processing (deconvolution using the nearest neighbor algorithm with 40% hazel-removal factor, and background correction) xCellence software was used.

After determining suitable concentrations and incubation times for **Dg** derivatives to achieve their detectable intracellular accumulation, colocalization studies with specific cell organelle markers were performed. Specifically: ER-Tracker™ Blue-White (150–200 nM, 45–90 min), ER-Tracker™ Red (150 nM, 60 min), LysoTracker™ Blue DND-22 (70–100 nM, 30–60 min), LysoTracker™ Red DND-99 (70–100 nM, 30–45 min), and Cellmask™ Deep Red® (500 μg μL^{-1}, 10 min.) all from ThermoFisher Scientific (USA), and MitoView™ 405(20 nM, 10 min.) from Biotium. QCC were calculated using ImageJ Colocalization Colormap module from ≥8 cells.

5.8 Cell death analysis in lung adenocarcinoma cells

The A549 and MRC-5 cells were seeded at the density of 1.25 × 10^5 cells per one mL into wells of 6-well plates and incubated at standard conditions for 24 h. Then, the cells were treated with **FD10** (0.75–3 μM), **FD9** (2.5–10 μM), and **Dg** (300 nM). After 24 and 48 h, the cells were harvested and processed according to the manufacturer's protocol.[76,77] Briefly, the cells were washed with PBS, trypsinized, centrifuged twice at 500×*g* for 2 min., and resuspended in 100 μL of annexin-binding buffer. Then, the cells were incubated either with 5 μL of Alexa Fluor® 488 Annexin V and 1 μL of propidium iodide ("green-emitting annexin", Thermo Fisher Scientific, USA) for 15 min. (For **FD10**) or with 5 μL of CFBlue Annexin V for 15 min. And with 5 μL of 7-aminoactinomycin D ("blue-emitting annexin", Immunostep, Spain) for 5 min. (for **FD9**), at room temperature. Then, the mixtures were diluted in 400 μL of annexin-binding buffer and analyzed by flow cytometer BD FACSAria III using lasers and filters as provided in Table 8. The percentage of apoptotic and necrotic cells was determined by BD FACSDiva 8 software. The means and the standard deviations were calculated (GraphPad Prism 8) from three independent experiments ($n = 3$).

5.9 Cell cycle and cell death analysis in leukemic lymphoblasts

Cell cycle and apoptosis analyses have been described previously [in ref. 78]. In brief, CCRF-CEM cells were exposed to compounds for 24 h, then harvested, washed with cold PBS, fixed in cold 70% ethanol, treated with RNase (0.5 mg mL^{-1}), and stained with propidium iodide (0.1 mg mL^{-1}). The samples were measured by flow cytometry using a 488 nm single-beam laser using the FACSCalibur (Becton Dickinson), and the data were analyzed by ModFitLT software (Verity) and CellQuest software.

Author contributions

Conceptualization – M. J., P. D., S. R., T. R., P. D., M. H.; formal analysis – J. B., M. J., M. K., I. K., J. F., S. G.; funding acquisition – T. R., M. J., P. D., M. H., S. R., P. D. V. S.; investigation – J. B., M. K., J. Š., M. J., S. G., I. K., J. F., S. R.; methodology – J. B., M. K., J. Š., M. J., S. G., I. K., J. F., S. R.; project administration – T. R., M. J., P. D., M. H., S. R., P. D.; resources – T. R., M. J., P. D., M. H., S. R., P. D. V. S.; supervision – T. R., M. J., P. D., S. R., P. D. V. S.; visualization – J. B., M. J.; writing – original draft – J. B., S. R., M. J.; writing – review and editing – P. D.; T. R., M. H.; P. D., V. S., J. Š.; I. K.; J. F., M. J., S. R. All authors have given approval to the final version of the manuscript.

Conflicts of interest

The authors declare no competing financial interest.

Abbreviations

DgA	Azido-terminated digitoxin analogue
AP	[3-(Azidomethyl)-5-hydroxyphenyl] methanamine
A549	Cells derived from lung adenocarcinoma
CCRF-CEM	Acute lymphoblastic leukemia
CGs	Cardiac glycosides
CuAAC	Azidoalkyne cycloaddition
Dg	Digitoxin
ER	Endoplasmic reticulum
FEIR	Fluorescence emission intensity ratio of conjugate and its respective fluorophore
IC_{50}	Half-maximal inhibitory concentration
MAPK	Mitogen-activated protein kinase
MEK	Mitogen-activated protein kinase
MRC-5	Noncancerous lung fibroblasts
NKA	Na^+/K^+-ATPase
PI3K	Raf, proto-oncogene serine/threonine kinase
Ras	Small GTPase
Src	Non-receptor tyrosine kinase
TAMRA	5(6)-Carboxytetramethylrhodamine
QCC	Quantitative colocalization coefficients
BODIPY	Boron-dipyrromethene
Raf	Rapidly accelerated fibrosarcoma kinase

Data availability

The data supporting this article have been included as part of the supplementary information (SI). Supplementary information: ^1H, ^{13}C NMR and HRMS spectra, UV-vis and fluorescence spectra, molecular docking of **Dg** conjugates into NKA, intracellular localization of **Dg** conjugates in A549 and MRC-5 cells

and colocalization analyses with subcellular markers, cytotoxicity of **Dg** derivatives in cell monolayers and cell spheroids, apoptosis induction, cell cycle analysis, molecular dynamics. See DOI: https://doi.org/10.1039/d6ra03722d.

Acknowledgements

The biological part of this study was supported in part by the infrastructural projects CZ-OPENSCREEN (LM2023052) and EATRIS-CZ (LM2023053) from the Ministry of Education, Youth and Sports of the Czech Republic, and by the project PerMed:T2BA – Personalised Medicine: From Translational Research into Biomedical Applications (TN02000109), co-financed with the state support of the Technology Agency of the Czech Republic within the National Centres of Competence Programme. Computational resources were provided by the e-INFRA CZ project (ID: 90254), supported by the Ministry of Education, Youth and Sports of the Czech Republic. This work was supported from the grant of Specific university research A1_FPBT_2022_001.

References

1 World Health Organization, https://www.who.int/news-room/fact-sheets/detail/cancer, accessed December 2024.
2 M. Malvezzi, C. Santucci, P. Boffetta, G. Collatuzzo, F. Levi, C. La Vecchia and E. Negri, European cancer mortality predictions for the year 2023 with focus on lung cancer, *Ann. Oncol.*, 2023, **34**, 410–419, DOI: 10.1016/j.annonc.2023.01.010.
3 C. Santucci, S. Mignozzi, M. Malvezzi, P. Boffetta, G. Collatuzzo, F. Levi, C. La Vecchia and E. Negri, European cancer mortality predictions for the year 2024 with focus on colorectal cancer, *Ann. Oncol.*, 2024, **35**, 208–316, DOI: 10.1016/j.annonc.2023.12.003.
4 H. Xue, J. Li, H. Xie and Y. Wang, Review of drug repositioning approaches and resources, *Int. J. Biol. Sci.*, 2018, **14**, 1232–1244, DOI: 10.7150/ijbs.24612.
5 S. Pushpakom, F. Iorio, P. A. Eyers, K. J. Escott, S. Hopper, A. Wells, A. Doig, T. Guilliams, J. Latimer, C. McNamee, A. Norris, P. Sanseau, D. Cavalla and M. Pirmohamed, Drug repurposing: progress, challenges and recommendations, *Nat. Rev. Drug Discovery*, 2019, **18**, 41–58, DOI: 10.1038/nrd.2018.168.
6 H. Reuter, S. A. Henderson, T. Han, R. S. Ross, J. I. Goldhaber and K. D. Philipson, The Na^+-Ca^{2+} exchanger is essential for the action of cardiac glycosides, *Circ. Res.*, 2002, **90**, 305–308, DOI: 10.1161/hh0302.104562.
7 M. Haas, H. Wang, J. Tian and Z. Xie, Src-mediated inter-receptor cross-talk between the Na^+/K^+-ATPase and the epidermal growth factor receptor relays the signal from ouabain to mitogen-activated protein kinases, *J. Biol. Chem.*, 2002, **277**, 18694–18702, DOI: 10.1074/jbc.M111357200.
8 M. Haas, A. Askari and Z. Xie, Involvement of Src and epidermal growth factor receptor in the signal-transducing function of Na^+/K^+-ATPase, *J. Biol. Chem.*, 2000, **275**, 27832–27837, DOI: 10.1074/jbc.M002951200.
9 I. Prassas, G. S. Karagiannis, I. Batruch, A. Dimitromanolakis, A. Datti and E. P. Diamandis, Digitoxin-induced cytotoxicity in cancer cells is mediated through distinct kinase and interferon signaling networks, *Mol. Cancer Ther.*, 2011, **10**, 2083–2093, DOI: 10.1158/1535-7163.MCT-11-0421.
10 D. J. McConkey, Y. Lin, L. K. Nutt, H. Z. Ozel and R. A. Newman, Cardiac glycosides stimulate Ca^{2+} increases and apoptosis in androgen-independent, metastatic human prostate adenocarcinoma cells, *Cancer Res.*, 2000, **60**, 3807–3812.
11 A. Miyakawa-Naito, P. Uhlén, M. Lal, O. Aizman, K. Mikoshiba, H. Brismar, S. Zelenin and A. Aperia, Cell signaling microdomain with Na,K-ATPase and inositol 1,4,5-trisphosphate receptor generates calcium oscillations, *J. Biol. Chem.*, 2003, **278**, 50355–50361, DOI: 10.1074/jbc.M305378200.
12 Z. Yuan, T. Cai, J. Tian, A. V. Ivanov, D. R. Giovannucci and Z. Xie, Na/K-ATPase tethers phospholipase C and IP3 receptor into a calcium-regulatory complex, *Mol. Biol. Cell*, 2005, **16**, 4034–4045, DOI: 10.1091/mbc.E05-04-0295.
13 J. Liu, R. Kesiry, S. M. Periyasamy, D. Malhotra, Z. Xie and J. I. Shapiro, Ouabain induces endocytosis of plasmalemmal Na/K-ATPase in LLC-PK1 cells by a clathrin-dependent mechanism, *Kidney Int.*, 2004, **66**, 227–241, DOI: 10.1111/j.1523-1755.2004.00723.x.
14 Y. Xu, P. Marck, M. Huang, J. X. Xie, T. Wang, J. I. Shapiro, L. Cai, F. Feng and Z. Xie, Biased effect of cardiotonic steroids on Na/K-ATPase–mediated signal transduction, *Mol. Pharmacol.*, 2021, **99**, 217–225, DOI: 10.1124/molpharm.120.000101.
15 L. Chen, P. Jiang, J. Li, Z. Xie, Y. Xu, W. Qu, F. Feng and W. Liu, Periplocin promotes wound healing through the activation of Src/ERK and PI3K/Akt pathways mediated by Na/K-ATPase, *Phytomedicine*, 2019, **57**, 72–83, DOI: 10.1016/j.phymed.2018.12.015.
16 J. Schjøtt, H. M. Torgauten and T. K. Bjånes, Shortage of digitoxin and switching to digoxin in Norway: A retrospective study of blood samples submitted to a clinical pharmacology laboratory, *Basic Clin. Pharmacol. Toxicol.*, 2017, **121**, 74–77, DOI: 10.1111/bcpt.12770.
17 H. A. Elbaz, T. A. Stueckle, H. Y. L. Wang, G. A. O'Doherty, D. T. Lowry, L. M. Sargent, L. Wang, C. Z. Dinu and Y. Rojanasakula, Digitoxin and a synthetic monosaccharide analog inhibit cell viability in lung cancer cells, *Toxicol. Appl. Pharmacol.*, 2012, **258**, 51–60, DOI: 10.1016/j.taap.2011.10.007.
18 C. Mi, X. Cao, K. Ma, M. Wei, W. Xu, Y. Lin, J. Zhang and T. Wang, Digitoxin promotes apoptosis and inhibits proliferation and migration by reducing HIF-1α and STAT3 in KRAS mutant human colon cancer cells, *Chem. Biol. Interact.*, 2022, **351**, 109729, DOI: 10.1016/j.cbi.2021.109729.
19 Y. Xu, J. Li, B. Chen, M. Zhou, Y. Zeng, Q. Zhang, Y. Guo, J. Chen and J. Ouyang, Cardiac glycosides inhibit proliferation and induce apoptosis of human

hematological malignant cells, *Int. J. Clin. Exp. Pathol.*, 2016, **9**, 9268–9275.
20 Y. Lei, H. Gan, Y. Huang, Y. Chen, L. Chen, A. Shan, H. Zhao, M. Wu, X. Li, Q. Ma, J. Wang, E. Zhang, J. Zhang, Y. Li, F. Xue and L. Deng, Digitoxin inhibits proliferation of multidrug-resistant HepG2 cells through G_2/M cell cycle arrest and apoptosis, *Oncol. Lett.*, 2020, **20**, 1–9, DOI: 10.3892/ol.2020.11932.
21 M. López-Lázaro, N. Pastor, S. S. Azrak, M. J. Ayuso, C. A. Austin and F. Cortés, Digitoxin inhibits the growth of cancer cell lines at concentrations commonly found in cardiac patients, *J. Nat. Prod.*, 2005, **68**, 1642–1645, DOI: 10.1021/np050226l.
22 H. Y. L. Wang, W. Xin, M. Zhou, T. A. Stueckle, Y. Rojanasakul and G. A. O'Doherty, Stereochemical survey of digitoxin monosaccharides, *ACS Med. Chem. Lett.*, 2011, **2**, 73–78, DOI: 10.1021/ml100219d.
23 A. K. V. Iyer, M. Zhou, N. Azad, H. Elbaz, L. Wang, D. K. Rogalsky, Y. Rojanasakul, G. A. O'Doherty and J. M. Langenhan, A direct comparison of the anticancer activities of digitoxin MeON-neoglycosides and *O*-glycosides, *ACS Med. Chem. Lett.*, 2010, **1**, 326–330, DOI: 10.1021/ml1000933.
24 L. A. Arnold, P. Ranaivo and R. K. Guy, Synthesis and characterization of BODIPY-labeled colchicine, *Bioorg. Med. Chem. Lett.*, 2008, **18**, 5867–5870, DOI: 10.1016/j.bmcl.2008.07.068.
25 M. Jurášek, S. Rimpelová, E. Kmoníčková, P. Drašar and T. Ruml, Tailor-made fluorescent trilobolide to study its biological relevance, *J. Med. Chem.*, 2014, **57**, 7947–7954, DOI: 10.1021/jm500690j.
26 S. Rimpelová, M. Jurášek, L. Peterková, J. Bejček, V. Spiwok, M. Majdl, M. Jirásko, M. Buděšínský, J. Harmatha, E. Kmoníčková, P. Drašar and T. Ruml, Archangelolide: A sesquiterpene lactone with immunobiological potential from *Laserpitium archangelica*, *Beilstein J. Org. Chem.*, 2019, **15**, 1933–1944, DOI: 10.3762/bjoc.15.189.
27 H. Y. Zhang, W. Q. Xu, Y. Y. Zheng, E. Omari-Siaw, Y. Zhu, X. Cao, S. S. Tong, J. N. Yu and X. M. Xu, Octreotide-periplocymarin conjugate prodrug for improving targetability and anti-tumor efficiency: Synthesis, *in vitro* and *in vivo* evaluation, *Oncotarget*, 2016, **7**, 86326–86338, DOI: 10.18632/oncotarget.13389.
28 T. Gao, H. He, R. Huang, M. Zheng, F. F. Wang, Y. J. Hu, F. J. Jiang and Y. Liu, BODIPY-based fluorescent probes for mitochondria-targeted cell imaging with superior brightness, low cytotoxicity and high photostability, *Dyes Pigm.*, 2017, **141**, 530–535, DOI: 10.1016/j.dyepig.2017.03.009.
29 A. Loudet and K. Burgess, BODIPY dyes and their derivatives: syntheses and spectroscopic properties, *Chem. Rev.*, 2007, **107**, 4891–4932, DOI: 10.1021/cr078381n.
30 W. Sandtner, B. Egwolf, F. Khalili-Araghi, J. E. Sánchez-Rodríguez, B. Roux, F. Bezanilla and M. Holmgren, Ouabain binding site in a functioning Na^+/K^+ ATPase, *J. Biol. Chem.*, 2011, **286**, 38177–38183, DOI: 10.1074/jbc.M111.267682.
31 T. Jimenez, G. Sánchez and G. Blanco, Activity of the Na,K-ATPase α4 isoform is regulated during sperm capacitation to support sperm motility, *J. Androl.*, 2012, **33**, 1047–1057, DOI: 10.2164/jandrol.111.015545.
32 E. Alonso, M. F. Cano-Abad, A. J. Moreno-Ortega, J. Novalbos, J. Milla, A. G. García and A. Ruiz-Nuño, Nanomolar ouabain elicits apoptosis through a direct action on HeLa cell mitochondria, *Steroids*, 2013, **78**, 1110–1118, DOI: 10.1016/j.steroids.2013.07.010.
33 M. J. Song, C. I. Davis, G. G. Lawrence and S. S. Margulies, influence of cell viability on stretch-induced permeability of alveolar epithelial cell monolayers, *Cell. Mol. Bioeng.*, 2016, **9**, 65–72, DOI: 10.1007/s12195-015-0405-8.
34 C. J. Ketchem, C. D. Conner, R. D. Murray, M. DuPlessis, E. D. Lederer, D. Wilkey, M. Merchant and S. J. Khundmiri, Low dose ouabain stimulates Na-KATPase α1 subunit association with angiotensin II type 1 receptor in renal proximal tubule cells, *Biochim. Biophys. Acta*, 2016, **1863**, 2624–2636, DOI: 10.1016/j.bbamcr.2016.07.008.
35 R. A. Newman, Y. Kondo, T. Yokoyama, S. Dixon, C. Cartwright, D. Chan, M. Johansen and P. Yang, Autophagic cell death of human pancreatic tumor cells mediated by oleandrin, a lipid-soluble cardiac glycoside, *Integr. Cancer Ther.*, 2007, **6**, 354–364, DOI: 10.1177/1534735407309623.
36 P. Yang, D. G. Menter, C. Cartwright, D. Chan, S. Dixon, M. Suraokar, G. Mendoza, N. Llansa and R. A. Newman, Oleandrin-mediated inhibition of human tumor cell proliferation: Importance of Na,K-ATPase α subunits as drug targets, *Mol. Cancer Ther.*, 2009, **8**, 2319–2328, DOI: 10.1158/1535-7163.MCT-08-1085.
37 A. Katz, D. M. Tal, D. Heller, H. Haviv, B. Rabah, Y. Barkana, A. L. Marcovich and S. J. D. Karlish, Digoxin Derivatives with Enhanced Selectivity for the α2 Isoform of Na,K-ATPase: Effects on intraocular pressure in rabbits, *J. Biol. Chem.*, 2014, **289**, 21153–21162, DOI: 10.1074/jbc.M114.557629.
38 D. M. Tal, S. J. D. Karlish and H. E. Gottlieb, An NMR study of new cardiac glycoside derivatives, *Magn. Reson. Chem.*, 2016, **54**, 260–262, DOI: 10.1002/mrc.4380.
39 J. Dai, X. Xue, X. Jiang, X. Liu and P. Zhan, Advances in click chemistry for drug discovery and development, *Expert Opin. Drug Discovery*, 2025, **20**, 1327–1343, DOI: 10.1080/17460441.2025.2552146.
40 C. F. A. Gómez-Durán, I. García-Moreno, A. Costela, V. Martin, R. Sastre, J. Bañuelos, F. López Arbeloa, I. López Arbeloa and E. Peña-Cabrera, 8-PropargylaminoBODIPY: unprecedented blue-emitting pyrromethene dye. Synthesis, photophysics and laser properties, *Chem. Commun.*, 2010, **46**, 5103–5105, DOI: 10.1039/c0cc00397b.
41 R. Vanhoutte, J. P. Kahler, S. Martin, S. van Veen and S. H. L. Verhelst, Clickable Polyamine Derivatives as Chemical Probes for the Polyamine Transport System, *ChemBioChem*, 2018, **19**, 907–911, DOI: 10.1002/cbic.201800043.
42 Y. Li, P. Schaffer and D. M. Perrin, Dual isotope labeling: conjugation of 32P-oligonucleotides with 18F-aryltrifluoroborate *via* copper(I) catalyzed cycloaddition,

Bioorg. Med. Chem. Lett., 2013, **23**, 6313–6316, DOI: 10.1016/j.bmcl.2013.09.064.

43 M. Börgardts, K. Verlinden, M. Neidhardt, T. Wöhrle, A. Herbst, S. Laschat, C. Janiak and T. J. J. Müller, Synthesis and optical properties of covalently bound Nile Red in mesoporous silica hybrids – comparison of dye distribution of materials prepared by facile grafting and by co-condensation routes, *RSC Adv.*, 2016, **6**, 6209–6222, DOI: 10.1039/C5RA22736D.

44 H. Hettegger, I. Sumerskii, S. Sortino, A. Potthast and T. Rosenau, Silane Meets Click Chemistry: Towards the Functionalization of Wet Bacterial Cellulose Sheets, *ChemSusChem*, 2015, **8**, 680–687, DOI: 10.1002/cssc.201402991.

45 R. Yan, E. El-Emir, V. Rajkumar, M. Robson, A. P. Jathoul, R. B. Pedley and E. Årstad, One-pot synthesis of an 125I-labeled trifunctional reagent for multiscale imaging with optical and nuclear techniques, *Angew. Chem., Int. Ed.*, 2011, **50**, 6793–6795, DOI: 10.1002/anie.201102072.

46 T. Morisaki, M. Denda, J. Yamamoto, D. Tsuji, T. Inokuma, K. Itoh, A. Shigenaga and A. Otaka, An *N*-sulfanylethylanilide-based traceable linker for enrichment and selective labelling of target proteins, *Chem. Commun.*, 2016, **42**, 6911–6913, DOI: 10.1039/C6CC01229A.

47 E. Palao, A. R. Agarrabeitia, J. Bañuelos-Prieto, T. A. Lopez, I. Lopez-Arbeloa, D. Armesto and M. J. Ortiz, 8-Functionalization of Alkyl-Substituted-3,8-Dimethyl BODIPYs by Knoevenagel Condensation, *Org. Lett.*, 2013, **15**, 4454–4457, DOI: 10.1021/ol401993p.

48 S. Zhu, J. Zhang, G. Vegesna, A. Tiwari, F. T. Luo, M. Zeller, R. Luck, H. Li, S. Green and H. Liu, Controlled Knoevenagel reactions of methyl groups of 1,3,5,7-tetramethyl BODIPY dyes for unique BODIPY dyes, *RSC Adv.*, 2012, **2**, 404–407, DOI: 10.1039/C1RA00678A.

49 X. Zhang, S. Zhang, S. Zhao, X. Wang, B. Liu and H. Xu, Click Chemistry in Natural Product Modification, *Front. Chem.*, 2021, **17**, 774977, DOI: 10.3389/fchem.2021.774977.

50 M. Laursen, L. Yatime, P. Nissen and N. U. Fedosova, Crystal structure of the high-affinity Na^+,K^+-ATPase ouabain complex with Mg^{2+} bound in the cation binding site, *Proc. Natl. Acad. Sci. U. S. A.*, 2013, **110**, 10958–10963, DOI: 10.1073/pnas.122230811051.

51 M. Laursen, J. L. Gregersen, L. Yatime, P. Nissen and N. U. Fedosova, Structures and characterization of digoxin- and bufalin-bound Na^+,K^+-ATPase compared with the ouabain-bound complex, *Proc. Natl. Acad. Sci. U. S. A.*, 2015, **112**, 1755–1760, DOI: 10.1073/pnas.1422997112.

52 R. Kanai, F. Cornelius, B. Vilsen and C. Toyoshima, Cryoelectron microscopy of Na^+,K^+-ATPase in the two E2P states with and without cardiotonic steroids, *Proc. Natl. Acad. Sci. U. S. A.*, 2022, **119**, e2123226119, DOI: 10.1073/pnas.212322611954.

53 The Human Protein Atlas, https://www.proteinatlas.org/ENSG00000163399-ATP1A1/cancer, accessed March 2026.

54 M. Cherniavsky-Lev, O. Golani, S. J. D. Karlish and H. Garty, Ouabain-induced internalization and lysosomal degradation of the Na^+/K^+-ATPase, *J. Biol. Chem.*, 2014, **289**, 1049–1059, DOI: 10.1074/jbc.M113.517003.

55 C. Gatto, C. M. McLoud and J. H. Kaplan, Heterologous expression of Na^+-K^+-ATPase in insect cells: intracellular distribution of pump subunits, *Am. J. Physiol. Cell Physiol.*, 2001, **281**, C982–C992, DOI: 10.1152/ajpcell.2001.281.3.C982.

56 L. Boff, L. Persich, P. Brambila, F. M. Ottoni, J. Munkert, G. S. Ramos, A. R. Soares Viana, W. Kreis, F. C. Braga, R. J. Alves, R. Maia de Pádua, N. F. Z. Schneider and C. M. O. Simões, Investigation of the cytotoxic activity of two novel digitoxigenin analogues on H460 lung cancer cells, *Anticancer Drugs*, 2020, **31**, 452–462, DOI: 10.1097/CAD.0000000000000872.

57 S. E. Meneses-Sagrero, L. A. Rascón-Valenzuela, R. Sotelo-Mundo, W. Vilegas, C. Velazquez, J. C. García-Ramos and R. E. Robles-Zepeda, Antiproliferative activity of cardenolides on cell line A549: structure–activity relationship analysis, *Mol. Diversity*, 2021, **25**, 2289–2305, DOI: 10.1007/s11030-020-10119-w.

58 A. Tchoryk, V. Taresco, R. H. Argent, M. Ashford, P. R. Gellert, S. Stolnik, A. Grabowska and M. C. Garnett, Penetration and uptake of nanoparticles in 3D tumor spheroids, *Bioconjugate Chem.*, 2019, **30**, 1371–1384, DOI: 10.1021/acs.bioconjchem.9b00136.

59 H. Eguchi, R. Akizuki, R. Maruhashi, M. Tsukimoto, T. Furuta, T. Matsunaga, S. Endo and A. Ikari, Increase in resistance to anticancer drugs involves occludin in spheroid culture model of lung adenocarcinoma A549 cells, *Sci. Rep.*, 2018, **8**, 15157, DOI: 10.1038/s41598-018-33566-w.

60 M. Wang, Y. Liu, X. Qian, N. Wei, Y. Tang and J. Yang, Downregulation of occludin affects the proliferation, apoptosis and metastatic properties of human lung carcinoma, *Oncol. Rep.*, 2018, **40**, 454–462, DOI: 10.3892/or.2018.6408.

61 H. Eguchi, R. Kimura, H. Matsunaga, T. Matsunaga, Y. Yoshino, S. Endo and A. Ikari, Increase in anticancer drug-induced toxicity by fisetin in lung adenocarcinoma A549 84 spheroid cells mediated by the reduction of claudin-2 expression, *Int. J. Mol. Sci.*, 2022, **23**, 7536, DOI: 10.3390/ijms23147536.

62 H. Eguchi, R. Kimura, S. Onuma, A. Ito, Y. Yu, Y. Yoshino, T. Matsunaga, S. Endo and A. Ikari, Elevation of anticancer drug toxicity by caffeine in spheroid model of human lung adenocarcinoma A549 cells mediated by reduction in claudin-2 and Nrf2 expression, *Int. J. Mol. Sci.*, 2022, **23**, 15447, DOI: 10.3390/ijms232415447.

63 M. Mustafa, R. Ahmad, I. Q. Tantry, W. Ahmad, S. Siddiqui, M. Alam, K. Abbas, Moinuddin, M. I. Hassan, S. Habib and S. Islam, Apoptosis: A comprehensive overview of signaling pathways, morphological changes, and physiological significance and therapeutic implications, *Cells*, 2024, **13**, 1838, DOI: 10.3390/cells13221838.

64 C. Garrido, L. Galluzzi, M. Brunet, P. E. Puig, C. Didelot and G. Kroemer, Mechanisms of cytochrome c release from

mitochondria, *Cell Death Differ.*, 2006, **13**, 1423–1433, DOI: 10.1038/sj.cdd.4401950.
65 L. Pan, Y. Zhang, W. Zhao, X. Zhou, C. Wang and F. Deng, The cardiac glycoside oleandrin induces apoptosis in human colon cancer cells *via* the mitochondrial pathway, *Cancer Chemother. Pharmacol.*, 2017, **80**, 91–100, DOI: 10.1007/s00280-017-3337-2.
66 R. Alford, H. M. Simpson, J. Duberman, G. C. Hill, M. Ogawa, C. Regino, H. Kobayashi and P. L. Choyke, Toxicity of organic fluorophores used in molecular imaging: Literature review, *Mol. Imaging*, 2009, **8**, 341–354, DOI: 10.2310/7290.2009.00031.
67 T. T. Nguyen, H. N. Nguyen, T. H. L. Nghiem, X.-H. Do, T. T. To, T. X. P. Do, D. L. Do, H. G. Nguyen, H. M. Nguyen, N. D. Nguyen, M. Q. Luu, T. N. Nguyen, T. B. N. Nguyen, V. T. Nguyen, V. T. Pham, U. T. T. Than and T. M. N. Hoang, High biocompatible FITC-conjugated silica nanoparticles for cell labeling in both *in vitro* and *in vivo* models, *Sci. Rep.*, 2024, **14**, 6969, DOI: 10.1038/s41598-024-57385-z.
68 S. Lee, S. Kang and S. Park, Comparison of Metabolic Profiles of Normal and Cancer Cells in Response to Cytotoxic Agents, *J. Korean Magn. Reson.*, 2017, **21**, 31–43, DOI: 10.6564/JKMRS.2017.21.1.31.
69 Jurášek, E. Dráberová, J. Řehulka, S. Gurská, A. Ivanova, P. Polishchuk, K. Ječmeňová, J. Fähnrich, A. Marešová, J. Tauchen, A. R. Romero, A. Dömling, M. Hajdúch, P. B. Drašar, P. Dráber and P. Džubák, Colchicine-BODIPY Probes: Evidence for the involvement of intracellular membranes in the targeting of colchicine to tubulin, *ACS Pharmacol. Transl. Sci.*, 2025, **8**, 1965–1985, DOI: 10.1021/acsptsci.5c00154.
70 Protein Data Bank, https://www.rcsb.org/, accessed February 2025.
71 K. Lindorff-Larsen, S. Piana, K. Palmo, P. Maragakis, J. L. Klepeis, R. O. Dror and D. E. Shaw, Improved side-chain torsion potentials for the Amber ff99SB protein force field, *Proteins*, 2010, **78**, 1950–1958, DOI: 10.1002/prot.22711.
72 GROMACS Tutorial, http://www.mdtutorials.com/gmx/complex/index.html, accessed February 2025.
73 V. Noskova, P. Dzubak, G. Kuzmina, A. Ludkova, D. Stehlik, R. Trojanec, A. Janostakova, G. Korinkova, V. Mihal and M. Hajduch, *In vitro* chemoresistance profile and expression/function of MDR associated proteins in resistant cell lines derived from CCRF-CEM, K562, A549 and MDA MB 231 parental cells, *Neoplasma*, 2002, **49**, 418–425.
74 BioByte, http://www.biobyte.com/index.html, accessed February 2025.
75 F. Piccinini, AnaSP: A software suite for automatic image analysis of multicellular spheroids, *Comput. Methods Programs Biomed.*, 2015, **119**, 43–52, DOI: 10.1016/j.cmpb.2015.02.006.
76 ThermoFisher Scientific, https://www.thermofisher.com/document-connect/document-connect.html?url=https://assets.thermofisher.com/TFS-Assets%2FLSG%2Fmanuals%2Fmp13242.pdf, accessed February 2025.
77 ImmunoStep, https://immunostep.com/wp-content/uploads/2023/04/TDS-ANXVF_EN.pdf, accessed February 2025.
78 A. Bourderioux, P. Nauš, P. Perlíková, R. Pohl, I. Pichová, I. Votruba, P. Džubák, P. Konečný, M. Hajdúch, K. M. Stray, T. Wang, A. S. Ray, J. Y. Feng, G. Birkus, T. Cihlář and M. Hocek, Synthesis and significant cytostatic activity of 7-hetaryl-7-deazaadenosines, *J. Med. Chem.*, 2011, **54**, 5498–5507, DOI: 10.1021/jm2005173.